Chapter 15
EPR of Primitive Organic Matter: A Tool for Astrobiology

Didier Gourier, Laurent Binet and Hervé Vezin

Abstract Insoluble organic matter (IOM) conserved in ancient sedimentary rocks and in carbonaceous meteorites can reveal valuable information about the origin of Life on Earth and on the birth of the Solar System, respectively. These IOMs are also reference materials for the search for possible organic traces of extinct life on Mars. The combination of continuous-wave and pulsed EPR of the radicals in IOM provided several markers distinguishing these materials and related to their histories. For terrestrial IOM, the EPR linewidth of the radicals is mostly determined by unresolved ^{1}H hyperfine interactions for IOM younger than 2500 million years (H-rich), and by dipolar interactions for older (H-depleted) IOM. The age of very primitive IOM could be estimated through the lineshape, which continuously evolves from Lorentzian to stretched Lorentzian upon ageing due to a change in the dimensionality of the radical spatial distribution. Nuclear spins within or near the radicals and the hyperfine interactions probed by pulsed EPR (through ESEEM and HYSCORE sequences) clearly distinguish meteoritic from terrestrial IOM. Radicals in meteorites are massively enriched in deuterium compared to terrestrial radicals, as a result of specific deuterium enrichment processes in the outer early Solar System. Meteoritic and terrestrial IOMs are also distinguished by the isotropic *vs* dipolar relative contributions in the ^{1}H hyperfine interactions and by the ^{13}C/^{1}H HYSCORE signal ratio. Strong ^{31}P and ^{14}N HYSCORE signals were detected in terrestrial IOM, which point to possible P and N rich biological precursors. The spin states of the radicals could also be determined either indirectly from the temperature dependence of the EPR intensity or directly by transient nutation spectroscopy. Meteoritic IOM, in addition to $S = 1/2$ radicals, specifically contains species with either triplet ground state or thermally excited triplet states, which are lacking in terrestrial IOM.

D. Gourier (✉) · L. Binet
Institut de Recherche de Chimie-Paris, CNRS, PSL Research University,
Chimie-Paristech-CNRS, 11 rue Pierre et Marie Curie, 75005 Paris, France
e-mail: didier.gourier@chimie-paristech.fr

H. Vezin
Laboratoire Spectrochimie Infrarouge et Raman, CNRS, University of Lille 1,
Villeneuve d'Ascq, France

A. Lund, M. Shiotani (eds.), *Applications of EPR in Radiation Research,*
DOI 10.1007/978-3-319-09216-4_15

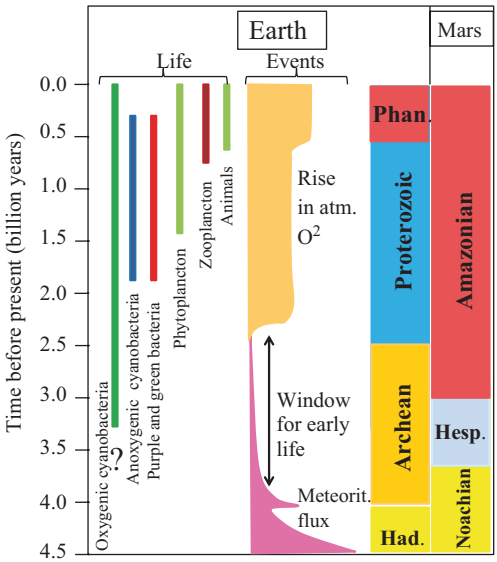

Fig. 15.1 Schematic diagram showing the different eons in Earth and Mars history, with the main geological and biological events on Earth. Had = Hadean; Phan = Phanerozoic; Hesp = Hesperian. Conditions of Mars during Noachian were compatible with life (atmosphere and water)

15.1 Introduction

Astrobiology makes use of all scientific disciplines to study life in the universe, including the origin of life on Earth, and the origin of the organic matter in the Solar System. All the planets and the Sun appeared 4560 million years (Myr) ago. It is generally agreed that life appeared rapidly on Earth, when ocean temperature decreased to about 80 °C [1, 2]. The main steps in history of Earth and its biosphere are schematized in Fig. 15.1. Although life emerged probably around 4000–3800 Myr ago, the most ancient putative traces of life on Earth are recorded in the form of carbonaceous microstructures fossilized in silicified sediments (cherts) deposited in ~3500 Myr-old seas. Although there is no doubt that the most primitive life was microbial in nature, the interpretation of these remains are complicated by the fact that very ancient rocks have often been subjected to high temperatures and (or) pressure (metamorphism). Also, even when sedimentary rocks are well preserved and have been subjected only to a moderate metamorphism, which is the case with several geological formations from Pilbara in Australia and Barberton in South Africa, the interpretation of these remains is further complicated by the possibility of more recent contaminations by endolithic microorganisms, weathering, hydrothermalism etc… [3–5]. In addition to this "syngeneity" problem, another important question is that of "biogenicity". As very ancient rocks are concerned, a part of the organic matter may be of chemical origin, such as decomposition of carbonates for example [6], or also of extraterrestrial origin (carbonaceous meteorites, interplanetary dust particles, comets). These extraterrestrial objects, which are among the most primitive of the solar system (4560 Myr), contain a significant amount of carbonaceous matter similar to that of terrestrial kerogens

[7]. Earth and Mars were intensively bombarded during the early history of the solar system (Fig. 15.1), so that considerable amounts of organic carbon have been deposited on these planets [8], with a fraction of it possibly fossilized in marine sediments. Although the meteoritic bombardments at the epoch of the most ancient preserved carbonaceous fossils on Earth (~3500 Myr) were much weaker than during the "Late Heavy Bombardment" event that occurred approximately 4100 to 3800 Myr ago, the possibility for extraterrestrial organic matter to be preserved in sediments is highly relevant for the search of fossilized organic carbon on Mars [9]. This is because the major part of this organic matter is exceptionally stable and for this reason is called *Insoluble Organic Matter* (IOM) in the geological literature. It would thus resist over geological timescales even under the harsh Martian surface conditions [9]. In the case of any possible discovery of organic matter preserved in the oldest Mars sediments, it would be crucial to assess its origin. Indeed, Early Mars was warmer and wetter during Noachian (Fig. 15.1), and it had sufficient water to fill impact craters and to give a small sea covering its northern hemisphere [10], in which both extraterrestrial IOM and IOM from fossilized microorganism could be preserved. The problematic is the same for the IOM of primitive Earth sediment, and the biologic origin of the most primitive fossilized carbonaceous microstructures has been vehemently debated in recent years [6, 11–13]. For all these reasons, it becomes of primary interest to develop non invasive techniques that will allow to detect biomarkers of primitive life in the fossil carbonaceous matter, and to assess its syngeneity with the host rock.

Also, in addition to their possible role as a source of organic matter on Early Earth, carbonaceous meteorites can be considered as fossils of the Solar System birth, 4560 Myr-ago. They come from parent bodies with size of the order of tens of kilometers, which were too small to undergo differentiation by partial melting. For this reason their elemental composition is the same as Sun except the most volatile elements. These parent bodies were heated by radioactive decay of short live radionucleides, giving variable degrees of aqueous alteration and thermal metamorphism [14, 15]. Despite these modifications which occurred after the accretion of the parent body, the IOM retained molecular and isotopic signatures of the pre-accretionary history in the protosolar nebula, or before the formation of this protosolar nebula (*ie* before 4560 Myr) [16–18].

Among all the possible spectroscopic methods to study the primitive IOM in the context of the origin of life, Raman spectroscopy is one of the most emblematic one, since its first use in paleobiology in the seventies [19, 20]. This technique is now sufficiently mature so that ESA/NASA ExoMars planetary mission (proposed for launch in 2018) will contain a miniaturized Raman spectrometer [21]. However, in addition to some pitfalls such as autofluorescence and laser heating of IOM by the incident laser beam, the latter is highly absorbed by the brown or dark rocks containing carbon (usually cherts), so that Raman spectroscopy is limited to the surface, and 3D Raman hyperspectral imaging is limited to depth smaller than 20 μm in samples [20]. In the perspective of combining complementary techniques for the analysis of fossilized IOM, EPR spectroscopy presents interesting characteristics that are not shared with other techniques. In particular

the radiation-matter interaction involved in magnetic resonance being of magnetic-dipolar nature (compared with electric-dipolar interaction for other spectroscopic techniques), the microwave radiation-interaction is so weak that the bulk rather than the surface of the sample is probed with EPR spectroscopy. In this chapter, we focus on the primitive Earth's oldest rocks containing IOM, and on IOM from carbonaceous meteorites. The rather good combination of sensitivity, spectral resolution and selectivity of EPR is well adapted to the identification of markers for the origin and the age of biogenic and extraterrestrial IOM. It is important to note that EPR in such Astrobiological context is only emerging, so that considerable work remains to be done before reaching an EPR's maturity equivalent to that of Raman spectroscopy. It is worth noticing that EPR of transition metal ions can also be used to search for biosignatures of the origin of life [22, 23], however this aspect of EPR is not treated in the present chapter.

15.2 EPR of IOM in the Context of Origin of Life

The insoluble organic matter (IOM), which corresponds to the definition of kerogens in contrast with extractable organic matter, is the form of mature carbonaceous matter that is preserved in ancient sedimentary rocks, such as coals for example [24]. Also, the IOM present in carbonaceous meteorites is often described as "kerogen-like" [7]. Only kerogens originating from the evolution of biological materials are relevant in the context of the origin of life on Earth and the search for traces of extinct life on Mars. Moreover these materials must be clearly distinguished from kerogens originating from chemical origin, such as Fischer-Tropsch reactions or decarbonatation of carbonate minerals, and also from interplanetary delivery. During evolution at geological timescales, the organic matter is subjected to cracking and aromatization-condensation reactions, with the progressive elimination of functional groups (H_2O, CO_2, …) and linkage between aromatic molecules, leading to an increasing stacking of aromatic sheets [24]. This evolution manifests itself by a decrease of O/C ratio (diagenesis) followed by a decrease of H/C ratio (catagenesis), giving a disordered carbonaceous network made of more or less branched, stacked and disoriented aromatic domains with sizes corresponding to less than ten fused rings. The next stage (metagenesis) corresponds to an increase of the size of aromatic stacks, with a further release of CO_2, CH_4, N_2 etc. Paramagnetic radicals are formed during this geological evolution, giving a single EPR line growing up during catagenesis (radical formation) and then decreasing during metagenesis (radical condensation). This transition occurs at $H/C \approx 0.5$ in the case of coals [25]. At the molecular scale, this evolution corresponds to a progressive loss of memory of the biological origin of this material. In the case of Archean cherts, identification of the biological precursors syngenetic with the sediment formation is complicated due to possible organic contaminations during the formation of sediments (interplanetary

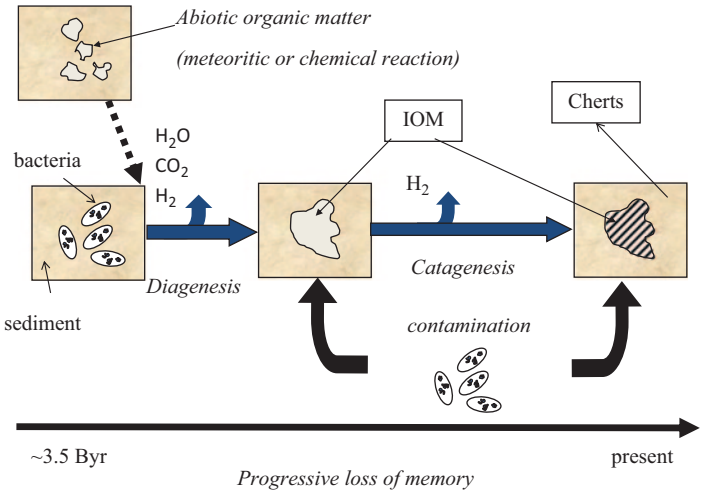

Fig. 15.2 Evolution of biological matter in sediments deposited in an Archean sea, including bacterial and abiotic contamination

material, abiotic IOM) or long after, by endolithic bacteria for example. All this evolution is schematized in Fig. 15.2.

In the case of Precambrian cherts, with ages ranging between ~3800 Myr and 540 Myr (Fig. 15.1), the IOM is generally very well preserved in microcrystalline siliceous rocks (cherts). In all cases, the EPR signal is a more or less symmetrical line at nearly free electron spin *g*-value. In this field range the signal is often superimposed to signals of defects and impurities of the mineral matrix, such as Fe^{III}, VO^{II}, E′ centres and $Al_{Si}°$ centres in SiO_2 (in Kröger-Vink notation) [22, 26]. At room temperature and at X-band, the EPR signal of radicals in IOM is superimposed with the $g_{//}$ component of E′ centre of the chert. This centre can be detected selectively by recording the signal 90°-*out-of-phase* with the modulation (Fig. 15.3a). The E′ centre spectrum can then be subtracted from the *in-phase* spectrum to give the pure IOM spectrum. In the case of carbonaceous meteorites, which contain a large fraction of magnetic minerals, the EPR spectrum is dominated by a broad (~130 mT) ferromagnetic resonance (FMR) signal, which masks the weak IOM signal [27]. The latter can be observed by isolating the IOM from the mineral matrix by a demineralizing treatment with concentrated HCl [28]. An example of EPR signal of IOM extracted by HF-HCl treatment of Orgueil and Murchison meteorites is given in Fig. 15.3b, where the narrow IOM line is superimposed to a broad and distorted FMR signal due to residual magnetic minerals [29].

Despite the single line character of the EPR spectrum of primitive IOM, a lot of information can be obtained (a) from the cw-EPR spectrum, such as *g*-factor, linewidth, lineshape, magnetism, (b) from analysis of the unresolved hyperfine interaction by using ENDOR or pulsed EPR methods, and (c) from direct measurement of

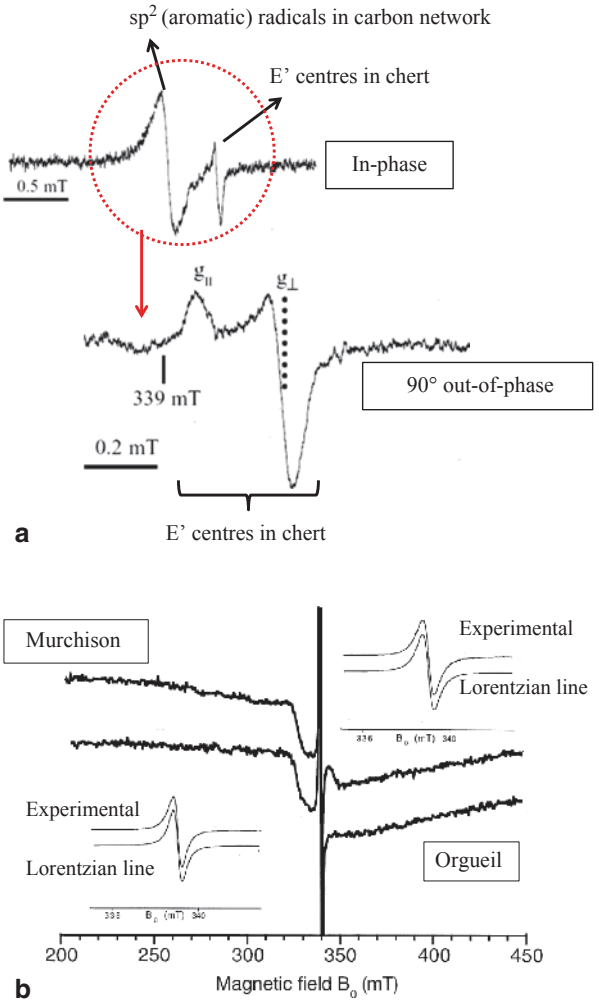

Fig. 15.3 Room temperature X-band EPR spectra of **a** 3500 Myr-old chert from Dresser Formation, Warrawoona Group, Pilbara Craton, Australia, recorded in-phase and 90° out-of-phase with the modulation, and **b** IOM from Orgueil and Murchison carbonaceous meteorites (~4500 Myr). Experimental condition: **a** Microwave power 0.02 mw (in-phase spectrum) and 2 mW (out-of-phase spectrum), **b** Microwave power 30 mW (main spectra) and 0.2 mW (inserts). Figure 15.3b is adapted from [29] with permission from Elsevier (2002)

electron spin states by nutation spectroscopy. All these data give information on the evolution stage of the IOM, its age and its origin as developed in next sections of this chapter (Table 15.1).

15.3 g-Factor and EPR Linewith

15.3.1 IOM of Meteorites

Curiously, it has been often argued that the abiotic IOM of carbonaceous meteorites is chemically similar to terrestrial type III kerogens [7], which are of biological

Table 15.1 Relation between EPR parameters and astrobiological information

Parameter	Method	Structural information	Astrobiological information
Linewidth	cw-EPR	H/C, radical concentration, disorder	Evolution of IOM, metamorphism
g-factor	cw-EPR	O/C and H/C of IOM	Evolution and alteration of IOM
Lineshape	cw-EPR	Spatial distribution of radicals	Evolution and dating of IOM
Intensity $I = f(T)$	cw-EPR	Magnetism	Origin of IOM (Earth versus interplanetary)
Electron spin value (S)	Nutation spectroscopy	Structure of aromatic radicals	Origin of IOM (Earth versus interplanetary)
^{1}H and ^{13}C hf interaction	HYSCORE (ESEEM)	Aliphatic branching of IOM radicals	Origin of IOM (Earth versus interplanetary)
^{31}P, ^{14}N, … hf interaction	HYSCORE (ESEEM)	Presence of heteroelements	Biosignatures
^{2}H hf interaction	HYSCORE (ESEEM)	D/H ratio	Origin of protosolar organic matter

origin! Based on their O/C and H/C ratio, terrestrial kerogens are classified in three types I, II and III. Kerogen type II originates from planktonic precursors deposited in open marine and fresh-water lacustrine environment, while type III originates from higher terrestrial plants deposited into lacustrine or marine settings [24]. Kerogen type I is due to different types of precursors in different sediment environments. As *g*-factor reflects the presence of heteroelements (mainly O) in the vicinity of radicals, it is closely related to the maturation degree of the IOM, reflected by its O/C and H/C ratios. Figure 15.4 shows variation of the *g*-factor versus O/C and H/C in kerogens of different origins [30], compared with data (in red) from Orgueil, Murchison and Tagish Lake meteorites [29, 31]. It appears that the similarity based on average chemical composition is also true for the environment of organic radicals. However it must be stressed that this similarity does not mean that protosolar IOM preserved in meteorites is of biological origin! It only indicates that radicals in abiotic IOM that preceded Earth and its life are of the same nature as radicals formed during maturation of IOM of biologic origin. The similarity of EPR lines and their *g*-factor for abiotic IOM (protosolar, 4500 Myr-old) and biogenic IOM clearly emphasizes the difficulty to find biosignatures of primitive life from the single EPR line of organic radicals.

15.3.2 IOM in Primitive Sedimentary Rocks

The complex evolution during geological timescale of the IOM fossilized in sedimentary rock can be studied by considering kinetics that controls the maturation

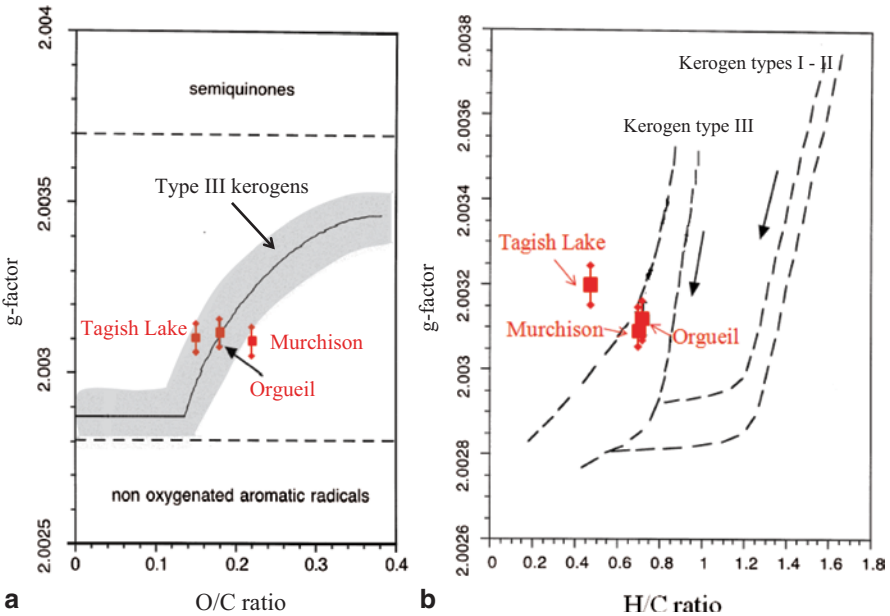

Fig. 15.4 **g**-factor versus O/C (**a**) and H/C (**b**) for radicals of IOM from Orgueil, Murchison and Tagish Lake meteorites (from refs [29] and [31]) compared with data from 31 type III kerogen samples of different origins (**a**, *grey area*, after ref [30]), and data for types I, II and III kerogens (**b**, *dashed lines*, from ref [25])

of kerogens, which is thought to be a first order kinetics [32, 33]. The amount of radicals N_{rad} created at time t is proportional to $N_{rad} \propto A\exp(-kt)$, with the kinetic constant given by:

$$k = A\exp\left(-\frac{E_a}{kT}\right) \tag{15.1}$$

where A is the collision constant (s^{-1}) and E_a the activation energy of maturation reactions. The intensity of the EPR line produced in IOM depends on both time and temperature $N_{rad}(t, T)$. This implies that the same amount of radicals, ie the same maturation stage, can be formed by using two different time-temperature couples (t_1, T_1) and (t_2, T_2) [34]:

$$t_1\exp\left(-\frac{E_a}{kT_1}\right) = t_2\exp\left(-\frac{E_a}{kT_2}\right) \tag{15.2}$$

This points out that ~1000 Myr at room temperature creates as many spins as 5 min at 670 °C. According to Eq. 15.2, an accelerated evolution of the IOM along geological timescale can be experimentally observed by step annealing treatment of cherts considered as very recent compared to the birth of Earth (4500 Myr). Figure 15.5 shows the evolution of EPR parameters of two cherts (396 and 45 Myr-old, respec-

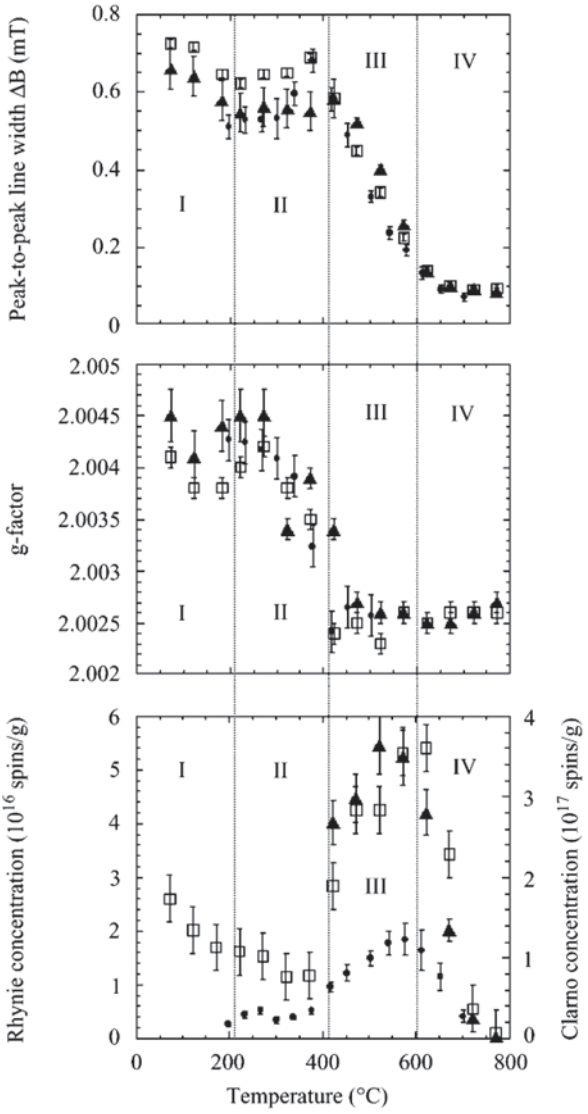

Fig. 15.5 Variation of room temperature EPR parameters of IOM radicals upon cumulative step heating treatment (15 min at each temperature) of cherts from the Rhynie formation, Aberdeenshire, Scotland (396 Myr-old) and the Clarno formation, Oregon, USA (45 Myr-old). *Top*: peak-to-peak linewidth ΔB; *middle*: *g*-factor; *bottom*: spin concentration. *Full triangles:* Rhynie chert; *Open squares*: Clarno chert under vacuum; *Full circles*: Clarno chert in ambient air. Adapted from [26] with permission from Springer (2008)

tively) upon cumulative step annealing treatments (15 min at each step) from room temperature to about 800 °C [26]. Four domains can be distinguished. In domain I, temperature is too low to produce significant variations of EPR parameters. Domain II corresponds to a decrease of the *g*-factor, reflecting a loss of oxygen in the form of H_2O and CO_2. This evolution is thus characteristic of *diagenesis* reactions observed on coals [25]. In domain III, the sharp decrease of the linewidth indicates a hydrogen loss and a significant increase of the amount of radicals. Indeed, as shown by spin echo experiments (see Sect. 15.5), the EPR linewidth is due to unresolved

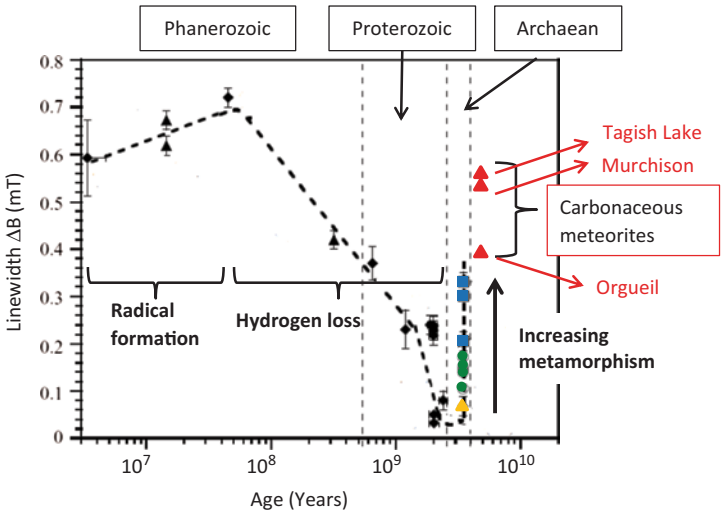

Fig. 15.6 Variation of the peak-to-peak EPR linewidth of IOM radicals in cherts of Phanerozoic, Proterozoic and Archean ages. Archean cherts are distinguished by their increasing metamorphic grade. These data are compared with those measured for the IOM of 4500 Myr-old carbonaceous meteorites. The *dashed line* is a guide for the eyes. Adapted from [26] with permission from Springer (2008)

hyperfine structure with ^{1}H nuclei of the IOM. Consequently, domain III can be related to *catagenesis* [24]. Finally, the high temperature domain IV is characterized by a constant linewidth and a decrease of the number of radicals, due to the condensation of aromatic groups observed in *metagenesis* [24].

Accordingly, EPR of IOM radicals in cherts of different geological ages will reflect the degree of evolution of this IOM. This is illustrated on Fig. 15.6, which shows the variation of the peak-to-peak linewidth ΔB of the IOM line in cherts with ages ranging from 2.9 Myr to ~3500 Myr [26]. According to Fig. 15.5, the decrease of ΔB with increasing age for Phanerozoic and Proterozoic cherts is due to the progressive hydrogen loss observed in domain III. However, for Archean cherts, which should correspond to domain IV, ΔB exhibits a broad distribution which cannot be due to a distribution of H/C ratio, as shown below by the lack of ^{1}H signal in HYSCORE spectra. It was found that in Archean IOM, the linewidth increases with the metamorphism of the rocks (yellow, green and blue symbols in Fig. 15.6). This indicates that the origin of line broadening of Archean IOM lines is different from the hyperfine broadening which characterizes Proterozoic and Phanerozoic cherts. However the observation of spin echoes (see Sect. 15.5 below) shows that the EPR lines are still inhomogeneously broadened, so that a broadening due to dipolar interactions between neighboring radicals appears the most likely for Archean IOM.

With this mechanism, the EPR linewidth in domain IV of Archean cherts is driven by the R^{-3} dependence of dipolar interactions between unpaired electron spins of radicals. Statistical theory predicts that the peak-to-peak linewidth of a Lorentzian line in a magnetically diluted spin system is related to the spin concentration N by [35]:

$$\Delta B = \frac{4\pi^2}{9} g\beta N \approx 8.12 \times 10^{-21} N \tag{15.3}$$

with N in cm^{-3} and ΔB in mT. As domain IV of the IOM evolution corresponds to a condensation of aromatic groups with a decrease of N, the fact that ΔB increases by a factor 5–7 shows that the surviving radicals concentrate in the form of shallow aggregates with local concentrations $N_{loc} > N$. These aggregates of radicals are probably localized in the boundary between ordered aromatic domains [36].

The EPR linewidth of IOM radicals in carbonaceous meteorites are shown in red in Fig. 15.6. Although these meteorites are among the most ancient objects of the solar system (4560 Myr), ΔB in the range 0.4–0.6 mT is the signature of a significant hydrogen content, in agreement with chemical analyses and with HYSCORE results shown in Sect. 15.5. These important hydrogen contents indicate that the parent bodies of these meteorites (which were destroyed by impacts shortly after their formation, giving meteorites) did not suffer from pronounced thermal episodes.

In principle, Fig. 15.6 shows that the EPR linewidth could give information on the evolution stage, and thus the age, of the fossil IOM. However this diagram must be used with caution because a linewidth $\Delta B \leq 0.3$ mT can correspond to two different periods (Proterozoic and Archean). For example, a 3500 Myr-old Archean chert containing fossil IOM with $\Delta B = 0.3$ mT corresponds either to bacteria fossilized 3500 Myr ago (syngenetic IOM) or to endolithic bacteria that lived in the rock ~500–700 Myr later (contamination). To assess syngeneity of the IOM (*i.e* dating IOM with respect to the host rock), we need a parameter which varies monotonically with the age of IOM.

15.4 Dating Primitive IOM by the EPR Lineshape

EPR spectra of IOM trapped in ancient sedimentary rocks and in carbonaceous meteorites are always characterized by a single symmetrical line with nearly free electron spin g-value. After considering the evolution of the linewidth in Sect. 15.3, we consider in this section the evolution of the lineshape, which exhibits three different types: Lorentzian, Lorentzian with Gaussian character, and stretched Lorentzian characterized by tails falling-off more slowly than pure Lorentzian. Four limit cases of lineshapes are shown in Fig. 15.7, where the magnetic field axis is normalized with respect to g-factor and linewidth. We observed that the lineshape varies continuously from Lorentzian-Gaussian to Lorentzian and to stretched Lorentzian with increasing stretching upon increasing age of the IOM of cherts [26]. Despite the fact that narrow Lorentzian-type EPR lines are generally associated to motional narrowing (in liquid) or to exchange narrowing (in solids) and are thus homogeneous [37], EPR lines of primitive IOM (cherts and meteorites) always give spin-echoes modulated by hyperfine interactions (ESEEM effect). This shows that EPR lines of IOM are inhomogeneously broadened by dipolar interactions [38, 39].

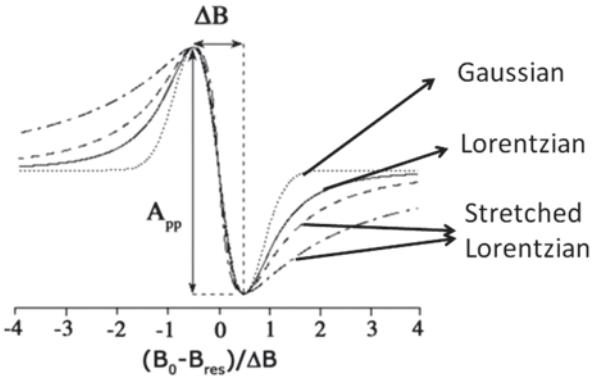

Fig. 15.7 Theoretical EPR lineshapes corresponding to limit cases of dipolar broadening. Gaussian lineshape corresponds to high spin concentration regime (electron spins or electron + nuclear spins). Lorentzian and the two stretched Lorentzian correspond to 3D, 2D and 1D electron spin distributions in diluted spin regime (see text). Adapted from [41] by permission from Mary Ann Liebert (2013)

The most detailed analysis of magnetic resonance lineshape of a diluted spin system randomly distributed in solid state has been given by Fel'dman and Lacelle [40]. They showed that the relaxation function $G_d(t)$ of the diluted spin system has the general form:

$$G_d(t) = B\exp(-at^{D/3}) \tag{15.4}$$

For electron spins, this function describes the decay with time t of the spin magnetization perpendicular to the magnetic field, after an infinitely short microwave pulse. Constant a depends linearly on the spin concentration, and D is the dimensionality of the spatial spin distribution, with $D=1$ for a linear distribution, $D=2$ for a distribution in a plane, and $D=3$ for a distribution in a volume. The EPR line is the first derivative of the Fourier transform of $G_d(t)$. The classical Lorentzian lineshape corresponds to the case $D=3$. The lower-dimensional distributions ($D<3$) give stretched Lorentzian. However there is no analytical expression for these lineshapes, which can only be calculated numerically. The two stretched Lorentzian shapes shown in Fig. 15.7 correspond to the limiting cases $D=2$ and $D=1$ (the most stretched line). In order to quantify the stretching character of EPR lines, it is more convenient to use a system of coordinates (X, Y) given by:

$$X = \left(\frac{B_0 - B_{res}}{\Delta B}\right)^2 \tag{15.5}$$

and:

$$Y = f(X) = \left(\frac{A_{pp}}{F(B_0 - B_{res})} \times \frac{B_0 - B_{res}}{\Delta B}\right)^{1/2} \tag{15.6}$$

where B_0, B_{res} and A_{pp} are the applied magnetic field, the field at the center of the line and the peak-to-peak amplitude, respectively. The function $F(B_0 - B_{res})$ represents the field derivative of a Lorentzian or a Gaussian absorption line. In this representation, the Lorentzian lineshape is represented by a straight line of equation:

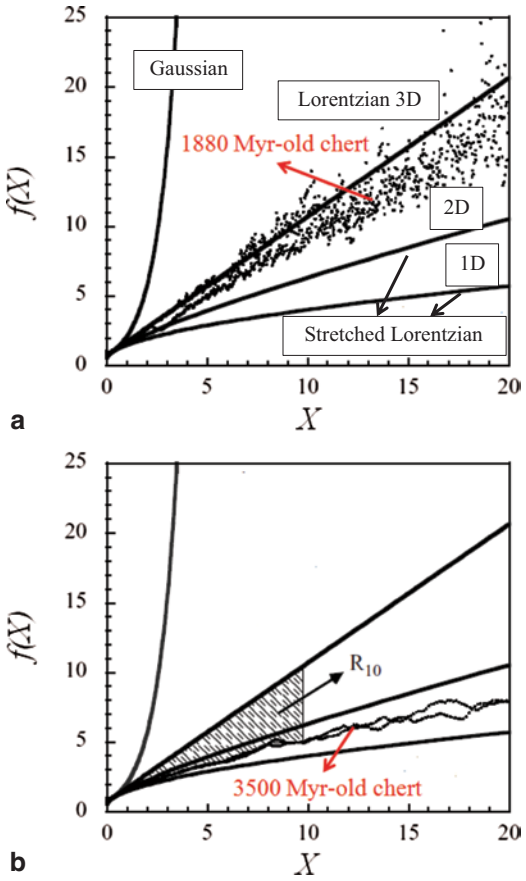

Fig. 15.8 EPR lineshape in a representation where a Lorentzian is linear with **a** experimental point for a 1880 Myr-old-chert (Gunflint formation, Ontario, Canada) and **b** a 3500 Myr-old chert (Dresser Formation, Warrawoona group, Australia). 3D, 2D and 1D represent the extreme case $D=3$, $D=2$ and $D=1$ for dimensionality of the spin distribution. The hatched area (R_{10}) between Lorentzian line and experimental points measures the deviation from the Lorentz shape function. Adapted from [26] with permission from Springer (2008)

$$Y = X + \frac{3}{4} \tag{15.7}$$

and the Gaussian lineshape is represented by an increasing exponential:

$$Y = \exp\left(X - \frac{1}{4}\right) \tag{15.8}$$

Stretched Lorentzian lineshapes are given by the (Y, X) representation of the first derivative of the Fourier transform of expression 15.4 with $D=2$ and $D=1$. The four limit cases of EPR lineshapes in this representation are shown in Fig. 15.8a.

Experimental spectra can be represented in this scheme by using Eq. 15.6 where $F(B_0 - B_{res})$ is measured from experimental points. The case of a 1880 Myr-old chert (Gunflint, Ontario, Canada) and a ~3500 Myr-old chert (Dresser Formation, Warrawoona Group, Australia) are given in Fig. 15.8a and b, respectively. We

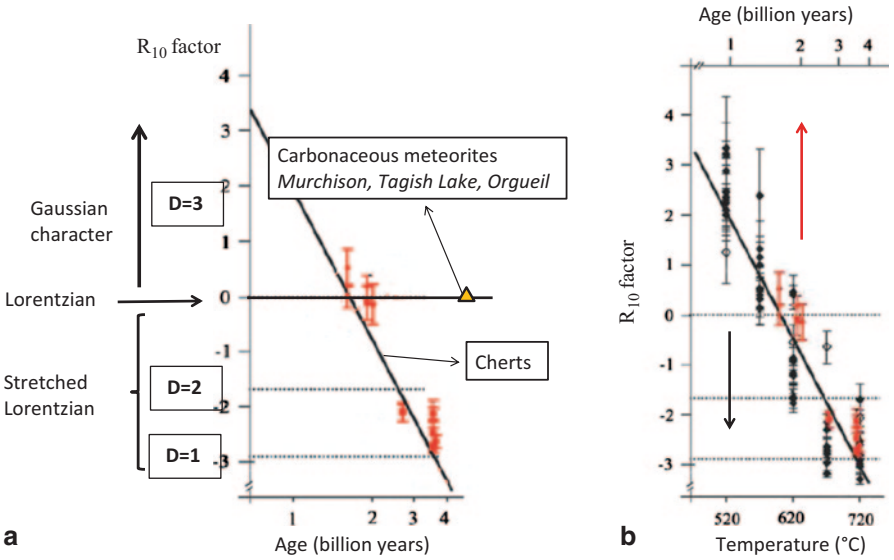

Fig. 15.9 **a** Variation of the lineshape factor R_{10} with the age of Precambrian chert samples (*red symbols*). Data for the IOM of three meteorites are given for comparison. **b** *Black symbols* and *bottom abscissa* represent the variation of R_{10} versus step annealing temperature for the 45 Myr-old Clarno chert (*open diamonds*) and for cyanobacteria (*full diamonds*). *Red symbols* and *top abscissa* represent the data of **a** for comparison. Adapted from [41] by permission from Mary Ann Liebert (2013)

quantified the experimental lineshape by defining a lineshape factor R_{10} given by (adapted from ref [26]):

$$R_{10} = \frac{1}{10}\int_0^{10}\left[f(X) - f_L(X)\right]dX \tag{15.9}$$

where $f_L(X)$ represents the Lorentzian line (Eq. 15.7). This lineshape factor corresponds to the algebraic surface between the experimental spectrum $f(X)$ and the Lorentzian line $f_L(X)$ (Fig. 15.8b). Integration is limited to $X=10$ in Eq. 15.9 because in most case, the signal-to-noise ratio becomes too low for $X \geq 10$, so that the integral may not converge for $X \rightarrow \infty$. The R_{10} factor is equal to 0 for a Lorentzian line, and any Gaussian or stretched Lorentzian character of the EPR line gives $R_{10} > 0$ or $R_{10} < 0$, respectively. For the limit case of diluted electron spin system without hyperfine broadening by ^{1}H nuclei, the limit values of R_{10} are $R_{10} = 0, -1.78$ and -2.95 for dimensionality of the spin distribution $D = 3$, 2 and 1, respectively. Details of data processing are given in [41].

R_{10} factors measured for a collection of Precambrian cherts coming from China, Canada, Australia and South Africa are shown in Fig. 15.9a [41]. It appears that the EPR line is nearly Lorentzian around 2000 Myr (Proterozoic), with a clear stretched character for Archean cherts. This indicates that the electron spins are homogeneously distributed ($D = 3$) in the IOM around 2000 Myr, and acquire a low

dimensional distribution ($2 \geq D \geq 1$) for Archean IOM (2500–3500 Myr). In order to get further insight into this effect, accelerated ageing experiment were performed by cumulative step annealing treatment as described above (Fig. 15.5) on a 45 Myr-old chert (Clarno Formation, Oregon, USA) containing a variety of fossil remains, and on cyanobacteria *microcoleus chtonoplastes* collected in the lake "La Salada de Chiprana" (Spain) [36]. The evolution of R_{10} factor with temperature for these two samples is shown as black symbols in Fig. 15.9b. Data below ~500 °C are not reported because the poor signal-to-noise ratio at lower temperature introduced too much error in R_{10} data processing. It appears that upon increasing step annealing temperature, R_{10} decreases linearly from R_{10} ~3 (Lorentzian with Gaussian character) to 0 (Lorentzian, $D=3$) and next to negative values corresponding to $D=2$ and $D=1$ for stretched Lorentzian [41]. The variation of R_{10} with age of Fig. 15.9a is also reported in Fig. 15.9b (red symbols, upper abscissa in Log scale). The temperature (T)-age (A) correlation (black line) corresponds to the following equation [26]:

$$T(^{\circ}C) = 353 \log A - 2650 \tag{15.10}$$

with A in years. This evolution shows that R_{10}varies continuously and not by steps as could be suggested by data of Fig. 15.9a. The positive R_{10} values of IOM younger than ~1500 Myr (step temperature T<~600 °C in the *T-A* correlation) corresponds to domain III in Fig. 15.5, where the line narrowing is due to hydrogen loss. This shows that the decreasing Gaussian character in the R_{10} variation is due to a decreasing unresolved hyperfine interaction with hydrogen nuclei. The Lorentzian shape observed around 2000 Myr indicates that radicals (small aromatic groups) are magnetically diluted and homogeneously distributed in the IOM. For Archean IOM (2500–3500 Myr), corresponding to step annealing temperatures T>~620 °C), the decreasing dimensionality of the spin distribution from $D=3$ to $D=1$ corresponds likely to the increasing size and increasing linkage of aromatic groups. This pushes the unpaired electron spins on the edges of these disordered aromatic networks, giving a bidimensional character to the spin distribution. Upon increasing ordering of these aromatic networks, leading to large aromatic sheets, defects become distributed along more or less linear edges, giving an apparent pseudo $D=1$ spin distribution. All this evolution of R_{10} from 0 to negative values corresponds to domain IV in Fig. 15.5. With the help of the age-temperature correlation, we obtain the following expression for the variation of R_{10} factor with the age of the IOM [41]:

$$R_{10} = \alpha \log A + \beta \tag{15.11}$$

with A in years and $\alpha = -9.0 \pm 0.3$ and $\beta = 83.0 \pm 2.9$. Expression 15.11 may be useful to assess the syngeneity of the IOM with respect to the host rock. For example if bacteria were fossilized in sediment of a 3500 Myr-old sea, we expect an EPR line of IOM with $R_{10} \approx -2.9$. Let us now consider a chert dated 3500 Myr by isotopic methods on minerals and giving an EPR line of IOM with $R_{10} \approx +1$, this strongly suggests that this IOM originates from endolithic bacteria that contaminated the rocks ~1200 Myr later, *ie* during Lower Proterozoic 2300 Myr ago.

It is interesting to note that IOM from carbonaceous meteorites, formed during the condensation of the protosolar nebula 4560 Myr ago, have an EPR lineshape factor R_{10} strictly equal to 0 (purely Lorentzian line), as shown in Figs. 15.3b and 15.9a. This is clearly related to the different history of the IOM in terrestrial and extraterrestrial conditions. In the first case, the evolution is governed by thermally activated processes, which can be even accelerated during metamorphic events. Extraterrestrial IOM has been submitted to very low temperature during the major part of its existence, to aqueous alteration when the radioactivity was sufficiently high to allow liquid water to circulate in the parent body, and to high flux of cosmic radiations from the Sun and the galaxy. The *g*-factor (Fig. 15.4) and the linewidth (Fig. 15.6) for meteoritic IOM are the signatures of high O/C and H/C ratios, indicating a low maturity, while the $R_{10}=0$ (Fig. 15.9a) is the signature of small aromatic radicals distributed in the volume of the IOM. These results for IOM radicals agree with ^{13}C NMR, FTIR, XANES, HRTEM and pyrolysis methods of meteoritic IOM, which give the image of a disordered IOM made of a network of small polyaromatic groups linked by highly branched and short aliphatic groups [42]. Despite these differences between meteoritic IOM and biogenic IOM fossilized in Archean cherts, it appears likely that any meteoritic input into the organic materials preserved in Archean sediments would be submitted to the same conditions of temperature as biological remains, so that the structure of the final IOM and the corresponding EPR spectra should be undistinguishable. In the perspective of searching for the origin of life on Earth and traces of extinct life on Mars, it is important to identify EPR markers which could discriminate biogenic IOM and IOM originating from an interplanetary input. As shown in the next section, such markers can be obtained from the hyperfine (hf) interaction between the unpaired spins and magnetic nuclei of radicals and their surroundings.

15.5 Searching for Nuclear Spin Signatures

Elements with spin $I=1/2$, such as Hydrogen ^{1}H (99.985 %), ^{13}C (1.11 %), ^{15}N (0.366 %) and ^{31}P (100 %), or with spin $I=1$, such as deuterium ^{2}H (0.0148 %, also noted D) and ^{14}N (99.63 %), can be present in IOM radicals or in their neighboring. Numbers in parenthesis are the natural abundances on Earth. However these abundances are generally different in extraterrestrial IOM. Hyperfine interaction (and quadrupolar interaction for nuclei with spin ≥ 1) is sensitive to the nature of chemical bond, the structure of electron ground state and to electron-nuclei distances, and thus gives direct information on the structure of IOM radicals. Also, the presence of particular heteroelements, of specific C–H bonds and isotopic compositions reflect the history of the IOM. This memory of the origin and evolution of IOM is recorded in the unresolved hf interactions, which can be measured by ENDOR and by pulsed EPR methods. Methods based on Electron spin echo envelope modulation (ESEEM) effect are well adapted to the very disordered and complex structure of IOM, because ESEEM allows the detection of all types of isotopes, and is particularly sensitive to those with small magnetic moment [43]. We used the two-dimensional version of

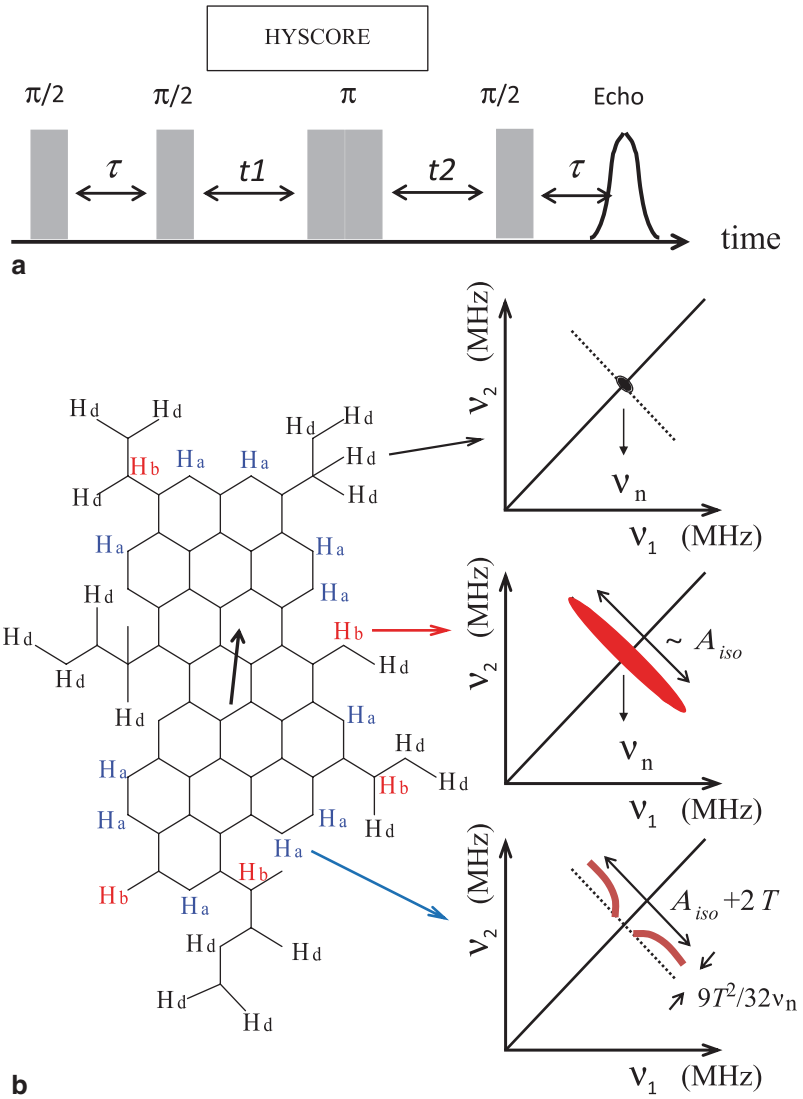

Fig. 15.10 **a** Pulse scheme for the HYSCORE experiment, **b** Schematic representation of a hypothetical branched polyaromatic fragment in IOM. The unpaired electron delocalized over the aromatic network is represented by an *arrow*. Three types of hydrogen atoms are distinguished: distant hydrogen (H_d), "benzylic" hydrogen (H_b) and aromatic hydrogen (H_a). The corresponding HYSCORE spectra are schematized on the *right*

4-pulse ESEEM, referred to as Hyperfine Sublevel Correlation (HYSCORE) method, corresponding to the pulse sequence shown in Fig. 15.10a [43, 44]. A first π/2 pulse that creates electron spin coherences, is followed by a second π/2 pulse after waiting time τ which transfers the coherence to neighboring nuclear spins. A third π pulse after time t_1 introduces correlations between m_I states of the two m_s states,

and these nuclear correlations are transferred back to electron spins by a π/2 pulse after time t_2, generating a spin echo after time τ. Waiting times t_1 and t_2 are varied stepwise at constant τ. The resulting two-dimensional set of echo modulations gives, after Fourier transform, a two-dimensional HYSCORE spectrum.

To illustrate the kind of information that can be obtained from hf interaction, let us consider in Fig. 15.10 a hypothetic polyaromatic radical, with the unpaired electron spin delocalized on a π-type molecular orbital made of carbon $2p_z$ orbitals (z perpendicular to the aromatic plane). The $2p_z$orbital on i^{th} carbon on the edge of polyaromatic radical bears an electron spin density ρ_i. Owing to the extremely disordered character of IOM, where polyaromatic groups may exhibit various sizes and shapes, and a variety of aliphatic branching, a rigorous interpretation of HYSCORE spectra is a difficult task. Whatever the size and shape of the polyaromatic group, the radicals always contain three main types of hydrogen atoms depending on their distance from the edge carbon atom C_i: (i) aromatic hydrogen (noted H_a) which are directly bonded to this carbon, (ii) hydrogen atoms in benzylic position (noted H_b) in an aliphatic group linked to this carbon, and (iii) more distant hydrogen atoms (noted H_d). From the point of view of ^1H hyperfine interaction, the polyaromatic radical can thus be considered as an association of C_i-H_a fragments and C_i-R fragments, with aliphatic groups $R = C(H_b)_2$-R′ or $CH_b(R')_2$ or $C(R')_3$, with carbon C_i bearing an electron spin density ρ_i. Distant hydrogen atoms H_d are localized in R′ fragments or in neighboring polyaromatic units. For a given H atom, nuclear modulation of the spin echo gives peaks located on (or close to) the ridge perpendicular to the diagonal of the HYSCORE spectrum and crossing it at the proton nuclear frequency ν_n. These peaks are characterized by frequency coordinates ν_- and ν_+ which depend on ν_n and two hyperfine parameters A and B [45, 46]:

$$\begin{aligned} \nu_+ &= \left[(\nu_n - A/2)^2 + (B/2)^2 \right]^{1/2} \\ \nu_- &= \left[(\nu_n + A/2)^2 + (B/2)^2 \right]^{1/2} \end{aligned} \tag{15.12}$$

with the hf interaction A given by $A = (\nu_-^2 - \nu_+^2)/2\nu_n$. It is the sum of the isotropic Fermi contact term A_{iso} and the dipolar term A_{dip}. In principle Eq. 15.12 is valid when A_{dip} is described by a point dipole approximation, which may not be rigorously true for a C_i-H_a fragment. For a spin density $\rho_i = 1$ on C_i atom, the Fermi contact term of a C_i-H_a fragment is characterized by the McConnell parameter Q_α which takes values in the range −67.3 to −84.1 MHz for a neutral radical [47]. The negative value is due to the negative spin density at the hydrogen nucleus originating from the spin polarization of the C-H bond by the electron in p_z orbital. The corresponding dipolar interaction contains three components $A_{dip,z} = 38$ MHz, $A_{dip,y} = -36$ MHz and $A_{dip,x} = -2.8$ MHz [48], with z axis along the C-H bond. The three hyperfine components of the C_i-H_a fragment are thus given by:

$$\begin{aligned} A_{i,x} &= \rho_i (Q_\alpha + A_{dip,x}) \\ A_{i,y} &= \rho_i (Q_\alpha + A_{dip,y}) \\ A_{i,z} &= \rho_i (Q_\alpha + A_{dip,z}) \end{aligned} \tag{15.13}$$

Thus even with a small spin density ρ_i, the hyperfine interaction with an aromatic hydrogen H_a is anisotropic. For a given ρ_i, the HYSCORE spectrum in an amorphous system gives peaks and ridges that are positively shifted from the anti-diagonal and exhibit a "horn shape" (Fig. 15.10). The splitting between the extrema of the ridge is equal to $A_{iso}+2T$, and the shift from the anti-diagonal is $9T^2/32\nu_n$, with $2T=A_{dip,\,z}$ [43, 49]. In disordered systems the distribution of ρ_i can lead to relatively complex HYSCORE lineshapes.

For branched C_i-R fragments, with aliphatic groups $R=C(H_b)_2$-R′ or $CH_b(R')_2$, the spin density at the hydrogen nucleus in benzylic position H_b is due to a direct spin transfer from the carbon p_z orbital, so that A_{iso} is large and positive:

$$A_{iso} = B_2 \cos^2\theta \tag{15.14}$$

with $B_2=+140$ to $+160$ MHz for a neutral π radical [47]. The angular dependence takes into account the efficiency of the spin transfer with the angle θ between the axis of the p_z carbon orbital and the orientation of the C-H bond. The dipolar interaction is smaller than 10 MHz [48], so that it can be neglected. Consequently, we expect for a H_b hydrogen $A_{i,\,x,y,\,z}\approx A_i\approx\rho_i{\cdot}A_{iso}$. For a given value of ρ_i, the spectrum is a pair of peaks along the anti-diagonal, with a splitting A_{iso}. In disordered IOM, we expect a distribution of ρ_i values so that all the peaks distributed along the anti-diagonal will overlap, giving a straight ridge. Finally, distant hydrogen atoms H_d are characterized by weak dipolar interactions, and they appear as a single peak at the proton frequency $\nu_n=14.5$ MHz. These three limit cases of HYSCORE lineshapes are illustrated in Fig. 15.10.

Figure 15.11 shows representative HYSCORE spectra at 9 K of three cherts dating 45 Myr (Clarno), 1880 Myr (Gunflint) and 3500 Myr (Dresser), and the IOM from Orgueil meteorite (4500 Myr). Tagish Lake meteorite gives the same type of spectrum as Orgueil [39], not shown here. These spectra show peaks and ridges of ^{1}H, ^{13}C, ^{31}P, ^{14}N and ^{29}Si nuclei, with the following characteristics.

15.5.1 ^{1}H and ^{13}C: Signatures of the Extraterrestrial/Terrestrial Origin?

We can first observe in Fig. 15.11 that the intensity of the ^{1}H-HYSCORE signal decreases with the age of the chert, which agrees with the EPR line narrowing with increasing age, resulting from the hydrogen loss during evolution of the IOM (Fig. 15.6). The fact that the ^{1}H signal vanishes in Achean cherts may be used to check the antiquity of the IOM and its syngeneity with the host rock. Indeed a late contamination would give IOM with a detectable proton signal. The lack of ^{1}H signal in the 3500 Myr-old Dresser chert clearly confirms that the dipolar broadening of its EPR line (Fig. 15.6) is a consequence of metamorphism and not the effect of an unresolved proton hyperfine interaction. The second important point is that the shape of ^{1}H-HYSCORE spectra of biogenic IOM (cherts) and abiotic IOM

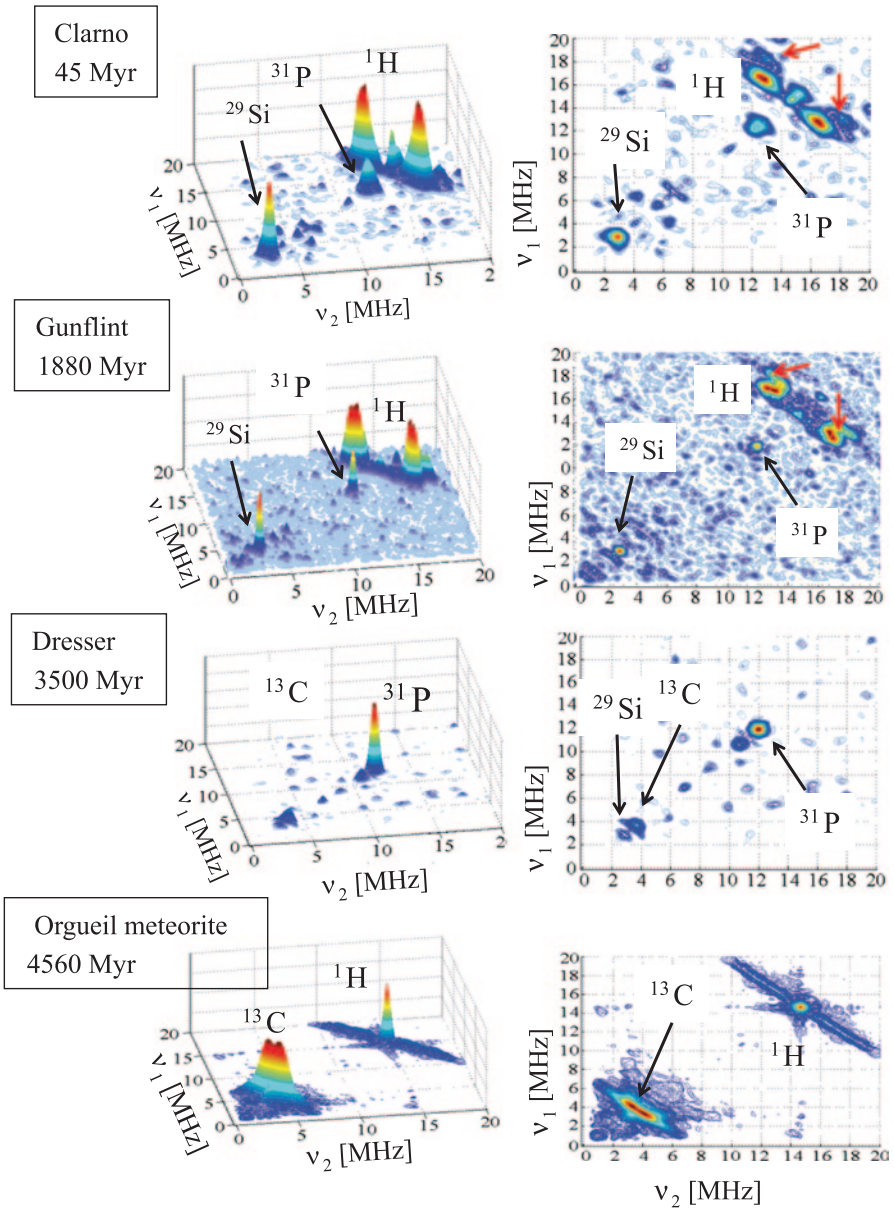

Fig. 15.11 HYSCORE spectra at 9 K and τ=136 ns for Clarno chert (45-Myr), Gunflint chert (1880 Myr) and Dresser chert (3500 Myr), and the IOM extracted from the Orgueil meteorite. Adapted from [39] with permission from Mary Ann Liebert (2013)

(meteorites) are different. The proton ridge is linear with a central peak at the proton frequency in meteoritic IOM, which indicates that the major part of hydrogen atoms of organic radicals is of "benzylic" type H_b and distant type H_d. This implies that most aromatic hydrogen atoms H_a in aromatic radicals have been exchanged by

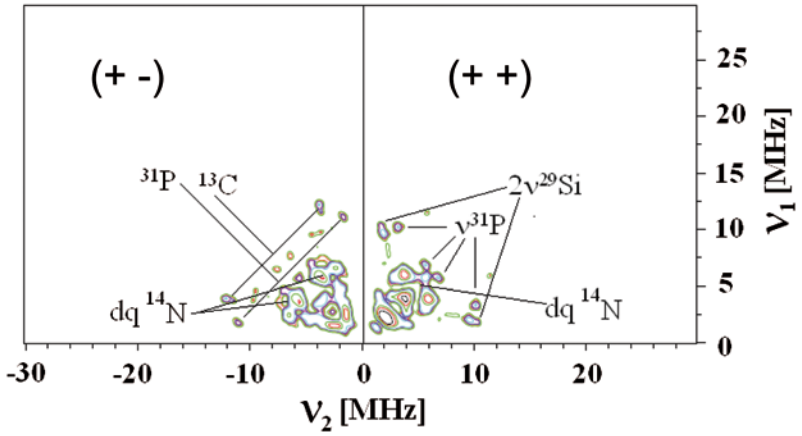

Fig. 15.12 HYSCORE spectrum at 4 K and $\tau = 130$ ns of the IOM extracted from the 3500 Myr-old chert of the Dresser Formation, Warrawoona Group, Australia. The (++) quadrant corresponds to $\nu_1 > 0$ and $\nu_2 > 0$, and the (+−) quadrant corresponds to $\nu_1 > 0$ and $\nu_2 < 0$. Double quantum transitions are noted dq. Adapted from [39] with permission from Mary Ann Liebert (2013)

aliphatic chains (the sources of H_b and H_d atoms). This result agrees with previous ^{13}C-NMR studies showing that meteoritic IOM is made of highly branched aromatic groups linked by short and branched aliphatic chains [50, 51]. Alternatively, proton ridges of biogenic IOM (cherts) exhibit a "horn shape" characteristic of anisotropic hyperfine interaction. In the case of the 1880 Myr-old Gunflint chert, analysis of ^{1}H-HYSCORE spectrum reveals the presence of several types of hydrogen atoms, the dominant one being characterized by hf parameters $A_{iso} \approx -3$ MHz and $T \approx +7$ MHz. The significant dipolar contribution and the negative value of A_{iso} show that these dominant hydrogen atoms are aromatic (H_a). In conclusion, aromatic radicals of biogenic IOM in cherts are poorly branched contrary to those of meteoritic IOM.

The same type of information can be obtained from the ^{13}C signal (frequency $\nu_n = 3.7$ MHz, natural Earth abundance 1.11 %) (Fig. 15.11). Surprisingly, this signal is very weak and narrow in IOM of cherts, and should not be confused with the ^{29}Si signal of the SiO_2 matrix ($\nu_n = 2.9$ MHz, natural Earth abundance 4 %). On the contrary, ^{13}C gives an intense ridge in meteoritic IOM. Ikoma et al. [52, 53] showed that ^{13}C/^{1}H intensity ratio increases with the number of equivalent carbon nuclei interacting with the electron spin. This ratio is clearly larger in meteorites than in cherts, which can be related to the highly (poorly) branched character of aromatic groups in the IOM of meteorites (of chert). The large number of carbon atoms at short distance of the polyaromatic group increases the probability for the electron spin to interact with a ^{13}C nucleus [39]. In order to detect ^{13}C signals in fossil IOM, it was necessary to increase the amount of IOM in the EPR cavity by removing the mineral part of the chert with the standard HF/HCl demineralization procedure [54]. The resulting HYSCORE spectrum for the IOM of the 3500 Myr-old Dresser chert is shown in Fig. 15.12 [39]. In the (+, −) quadrant corresponding to $|A| > 2\nu_n$, a doublet of ^{13}C peaks is centered at $|A/2| = 7.8$ MHz. The fact that two narrow peaks are observed instead of a broad frequency distribution indicates that the electron spin density is

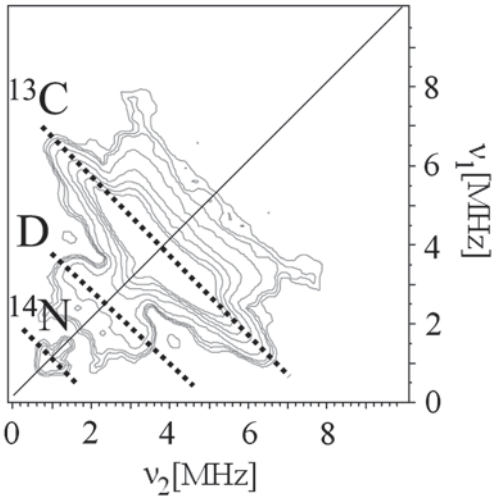

Fig. 15.13 Low frequency part of the HYSCORE spectrum at 10 K and $\tau = 136$ ns of the IOM extracted from the Orgueil meteorite. Adapted from [38] with permission from Elsevier (2008)

mainly localized on a single type of carbon atom in the edge of aromatic groups. This is clearly different from Meteoritic IOM, where the ^{13}C signal is localized in the (+, +) quadrant characterized by to $|A| < 2\nu_n = 7.4$ MHz (Figs. 15.11 and 15.13).

15.5.2 ^{31}P and ^{14}N: Signatures of Extinct Life?

Another prominent difference of hf signatures of the two types of IOM concerns heteroelements such as phosphorous and nitrogen. All cherts exhibit a peak at 12.2 MHz which is absent in meteorites (Fig. 15.11) [39]. It corresponds to a double frequency transition of ^{31}P ($\nu_n = 6.1$ MHz) occurring at $2\nu_n = 12.2$ MHz. Compared with ^{1}H signal, ^{31}P signal increases with the age of the IOM and dominates the HYSCORE spectrum for the oldest (Archean) IOM (Fig. 15.11). This double frequency ^{31}P peak, with no measurable hyperfine interaction, probably originates from phosphorous-rich nanophases in contact with the IOM [39]. Their systematic presence in cherts is an indication of their biologic origin, for example the degradation of nucleic acids (DNA, RNA). The attribution of this signal to ^{31}P is demonstrated by the study of IOM extracted for the 3500 Myr-old Dresser chert (Fig. 15.12). ^{31}P signals are clearly seen in both (+, +) and (+, −) quadrants. In the (+, +) quadrant, single frequency transitions of ^{31}P ($A_{iso} = 8$ MHz, $T = 1$ MHz) are seen in the vicinity of double frequency transitions of ^{29}Si. Two single frequency transitions of ^{31}P are also observed in the (+, −) quadrant, with $A \approx 13.8$ MHz. Such strong hf interactions are the indication of covalent C-P bonds at the periphery of IOM network [39]. On the opposite, ^{31}P signal is lacking in IOM from meteorites [38].

Differences between cherts and meteorites exist also in the ^{14}N-HYSCORE of extracted IOM. For meteorites, only a weak signal is observed at ^{14}N nuclear frequency ($\nu_n = 1.06$ MHz) with no measurable hyperfine interaction (Fig. 15.13),

while IOM from the 3500 Myr-old Dresser chert exhibits double quantum (dq) transitions in (+, +) and (+, −) quadrants, revealing at least two types of nitrogen atoms (Fig. 15.12). The fact that they have resisted to carbonization indicates that they are strongly bonded to the aromatic network. The presence of various types of nitrogen atoms in fossil IOM is also a strong indication of their biologic origin, which may result from the decomposition of proteins and nucleic acids, the latter being also responsible for the phosphorous signal.

15.5.3 Deuterium: A Marker of the Protoplanetary Disk Chemistry

In the following deuterium ^{2}H is noted D. Organic molecules of the interstellar medium are considerably enriched in deuterium ($D/H \approx 20{,}000 \times 10^{-6}$) relative to the solar hydrogen ($D/H = 25 \pm 5 \times 10^{-6}$) [55–57]. It was shown that this deuterium enrichment was produced by ion-molecule reactions at low temperature (down to 10 K) and at density $< 10^{3}$ H m^{-3} [58]. An important characteristic of meteoritic IOM is a systematic enrichment of the meteoritic IOM relative to terrestrial IOM [16], with reported values in the range $300–500 \times 10^{-6}$ [16, 59, 60]. However the origin of this enrichment is not clear as it is intermediate between the solar system abundance and interstellar abundance. To complicate the situation, it was recently shown that meteoritic IOM is highly heterogeneous in composition. Using Sims analyses, deuterium-rich hot-spots of micrometer sizes were found in the IOM, with D/H ratios up to 3200×10^{-6} [61, 62]. Two interpretations were proposed to account for the origin of these D-enriched regions [61, 62]: (1) Preserved interstellar D-rich molecules, (2) local concentrations of molecular species having the most exchangeable C–H bonds. In interpretation (2), the exchange would have taken place at the low temperature periphery of the protosolar disk, which exhibited a high degree of ionization caused by a massive irradiation from the young Sun [63].

With HYSCORE measurements on deuterium and hydrogen hyperfine interactions, it was possible to gain a deeper insight into the deuterium enrichment problem. Figure 15.13 shows the low frequency part of the HYSCORE spectrum of IOM extracted from the Orgueil meteorite. Deuterium signal is clearly observed between the broad ^{13}C ridge and the weak ^{14}N signal. By normalizing the intensity ratio D/H of IOM with a reference organic sample with known D/H, a high value $D/H = 15{,}000 \pm 5000 \times 10^{-6}$ was measured for Orgueil meteorite [38], which is close to interstellar values. It was shown quantitatively that organic radicals account for the entire excess of deuterium associated to the D-rich IOM hot spots [62]. Despite the extremely disordered character of meteoritic IOM, it was possible to localize the D-rich C-H bonds of the radicals. As shown in Sect. 15.5.1, the highly branched character of aromatic radicals implies that distant hydrogen atoms H_d and "benzylic"-type hydrogen atoms H_b dominate the ^{1}H-HYSCORE spectrum, as revealed by its linear shape (Fig. 15.12). Assuming that deuterium atoms partially exchange H_b hydrogen atoms, the ratio of hyperfine couplings should be equal to the ratio of nuclear *g*-factors:

$$\frac{A_H}{A_D} = \frac{g_{n,H}}{g_{n,D}} = 6.5 \tag{15.15}$$

From the values $\left|A_{H,\max}\right| = 12.3 \pm 0.2$ MHz and $\left|A_{D,\max}\right| = 2.0 \pm 0.3$ MHz measured from the lengths of hydrogen and deuterium ridges, a ratio $A_{H,\max} / A_{D,\max} = 6.2$ is obtained, very close to the expected value 6.5. Thus, assuming a "benzylic"position for deuterium atoms, their hyperfine coupling is calculated from Eqs. 15.14 and 15.15:

$$A_D \approx \rho_i \frac{g_{n,D}}{g_{n,H}} B_2 \cos^2\theta \tag{15.16}$$

This corresponds to the hyperfine coupling of a methylene deuterium adjacent to an aromatic carbon atom C_i bearing a spin density ρ_i in its p_z orbital. Hydrogen interaction shows that $\rho_i \leq 0.12$. As aromatic radicals are more or less stacked, angle θ should be closed to 30° for an aliphatic chain fixed on C_i carbon. With B_2 in the range 140–168 MHz [47], a deuterium coupling 1.9 MHz$< \left|A_{D,\max}\right| <$2.3 MHz is prediced, in good agreement with the experimental value 2.0 ± 0.3 MHz.

This analysis shows that the considerable deuterium excess of meteoritic IOM is mostly localized in "benzylic" positions of branched aliphatic chains fixed to the aromatic radicals [38]. The energy of the C-H_b bond (≈40 kcal/mol) is much smaller than that of the C-H_a bond (≈110 kcal/mol) [64]. This indicates that the deuterium atoms occupy the most exchangeable C-H bonds [38]. The temperature corresponding to the experimental D/H ratio of 15000×10^{-6} for the radicals is estimated to about 35 K, which is obtained in the outer regions of the protosolar disk at distances from the young Sun corresponding to the present day orbits of Kuiper Belt objects of the solar system [62]. It has been proposed that the heterogeneous composition of meteoritic IOM is the consequence of the accretion, on the parent body of meteorites, of two families of IOM particles [65]. The more abundant family is deuterium and radical poor, while the less abundant one contains a high quantity of D-rich particles (hot-spots) carried by radicals. In this model, proto-IOM grains localized in the inner and warm part of the disk are characterized by low D/H values. A small fraction of them could be brought by turbulences in the cold outer regions of the disk submitted to intense UV irradiation. Radicals could have formed and enriched in deuterium in this external proto-IOM, and next mixed by turbulences with internal proto-IOM to give the heterogeneous IOM found in carbonaceous meteorites. Particles with high quantity of D-rich radicals are less abundant than the other type of particles because of the large distance between the irradiated area and the inner accretion area.

15.6 Triplet State Radicals: Markers of Extraterrestrial IOM

In the preceding section, all the information on the IOM has been obtained from the hf interaction with ^{1}H, ^{2}H, ^{13}C, ^{31}P and ^{14}N nuclei in (or around) polyaromatic radicals. However this interaction gives no information on the size, the shape (and their distributions) of these radicals. As both fossil IOM and meteoritic IOM always give a single symmetric cw-EPR line with lineshape ranging from Lorentzian (with more or less Gaussian character) to stretched Lorentzian, it is natural to assume an electron spin $S = 1/2$ for all these aromatic radicals. This has been previously demonstrated for radicals in coals [52, 66–68] and in synthetic hydrogenated amorphous carbon [69, 70]. As shown below, this is also the case for the radicals of IOM in cherts. However the spin state of radicals has to be checked for meteorites owing to their complex history and the organic synthesis in conditions (temperature, pressure, irradiation) that do not exist on Earth. In the following we show that the major part of the radicals in meteoritic IOM possess a spin $S = 1$.

Radicals with $S = 1/2$ of terrestrial IOM are characterized by the spin Hamiltonian:

$$H(1/2) = \beta_e B_0 g S_z / \hbar + \sum_{k=1}^{m} \boldsymbol{S}\boldsymbol{A}_k \boldsymbol{I}_k - \beta_n \sum_{k=1}^{m} g_{n,k} B_0 I_{k,z} / \hbar \qquad (15.17)$$

where the three terms, from left to right, are the electron Zeeman, the hf and the nuclear Zeeman interactions, respectively. We neglect the quadrupolar interaction term, which occurs for nuclei with spin $I \geq 1$. Two additional terms are added for $S = 1$ diradicals:

$$H(1) = \beta_e B_0 g S_z / \hbar + \boldsymbol{S}_1 \boldsymbol{J} \boldsymbol{S}_2 + \boldsymbol{S}_1 \boldsymbol{D} \boldsymbol{S}_2 + \sum_{k=1}^{m} \boldsymbol{S}\boldsymbol{A}_k \boldsymbol{I}_k - \beta_n \sum_{k=1}^{m} g_{n,k} B_0 I_{k,z} / \hbar \qquad (15.18)$$

with $S_1 = S_2 = 1/2$. The additional interactions J and D are the exchange and the zero field splitting (ZFS) interactions, respectively. As the EPR spectrum of a radical is characterized by $2S$ lines, we should expect two lines for $S = 1$. Figure 15.14 shows a stick diagram representation of an $S = 1/2$ radical (blue interrupted line) and an $S = 1$ radical (red line), both with a nearly isotropic free spin g-factor. As the spin-orbit contribution to the ZFS is negligible (isotropic g-value close to 2.002), D can be written in the simple dipole-dipole approximation:

$$\begin{aligned} D_{dd} &= \frac{\mu_0}{4\pi\hbar} \frac{g^2 \beta_e^2}{r^3} (3\cos^2\theta - 1) \\ &= D'(3\cos^2\theta - 1) \end{aligned} \qquad (15.19)$$

where μ_0 stands for the permeability of vacuum, r for the electron-electron distance and θ for the angle between the magnetic field and the interconnection line between the two electron spins. The diradical gives a pair of EPR line at magnetic field

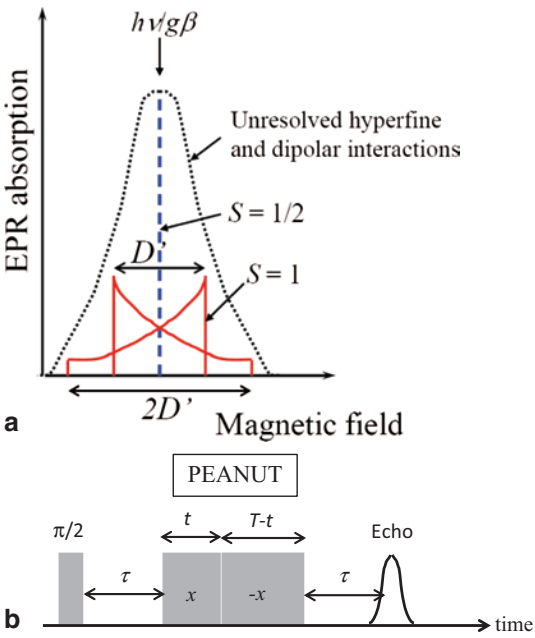

Fig. 15.14 **a** Schematic representation of an EPR absorption line (*dotted curve*) formed by the sum of $S=1/2$ radicals (*discontinuous line*) and $S=1$ diradicals (*full lines*) with unresolved structure due to broadening by proton hyperfine interactions and dipolar interactions between neighbouring defects. **b** Pulse sequence for the spin nutation (PEANUT) experiment. The time domain data are obtained by monitoring the echo intensity versus t-$T/2$. Nutation pulse length $T=2$ μs; $\tau=256$ ns

$B_0 \pm (3\cos^2\theta - 1)D'/2$ (with D' in magnetic field units). As the IOM is amorphous, θ spans all the possible values between 0 and π, so that the theoretical spectrum exhibits a typical "Pake pattern" with two prominent peaks at $B_0 \pm |D'|/2$ and two weak extrema at $B_0 \pm |D'|$ (Fig. 15.14). However these unrealistic stick spectra are broadened by hf interactions with ^{1}H nuclei, by dipolar interactions between neighbouring radicals, and by a distribution of interspin distances r, leading to a distribution of D' value. If $\langle D' \rangle$ is smaller than these two sources of broadening (i. e. $\langle D' \rangle < 11$ MHz), the composite spectrum may finally result in a simple unresolved and symmetrical line (dotted curve in Fig. 15.14).

15.6.1 Measurement of Spin States

In the absence of resolved ZFS structure, the spin states present in a solid can be measured by transient nutation spectroscopy, which is the rotational motion of the magnetization by the interaction of spins with the microwave (mw) field. The nutation frequency ω_{TN} is related to S by [71]:

$$\omega_{TN} = \left[S(S+1) - m_s(m_S+1)\right]^{1/2} g\beta B_1/\hbar \qquad (15.20)$$

An $S=1/2$ radical is thus characterized by $\omega_{TN} = g\beta B_1/\hbar$, and a $S=1$ radical by $\omega_{TN} = \sqrt{2}g\beta B_1/\hbar$, *i.e.* they differ by a factor $\sqrt{2}$. However this nutation frequency is often difficult to measure because of the rapid defocusing under B_1 field

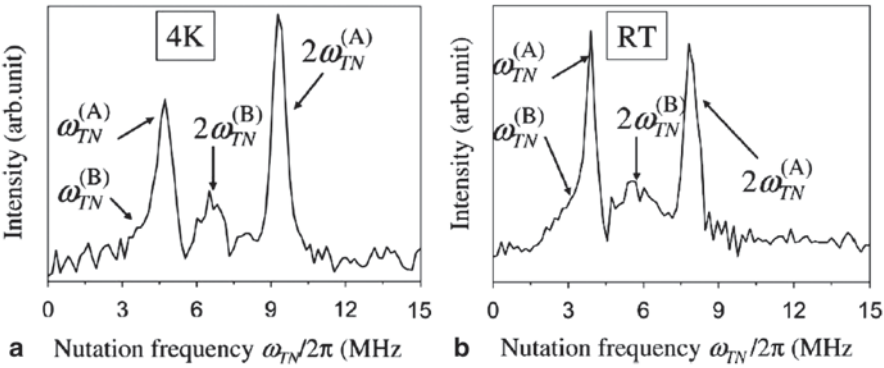

Fig. 15.15 Transient nutation (PEANUT) spectra at 4 K and room temperature of the IOM of the Orgueil meteorite. Adapted from [74] with permission from Elsevier (2011)

inhomogeneity. It can be refocused by detecting the so-called rotary echo [43, 72], whereby the nutation pulse of length T is divided into two parts of variable length t and T-t with opposite microwave phase. To minimize nuclear modulations at nuclear frequencies (ESEEM effect), the rotary echo can be detected via a spin-locked echo by the *Phase-inverted Echo-Amplitude detected NUTation* (PEANUT) method developed by Stoll et al. [73]. The corresponding pulse sequence is shown in Fig. 15.14b.

Nutation spectra at room temperature and at 4 K of the IOM of Orgueil meteorite are shown in Fig. 15.15 [74]. They show peaks at ω_{TN} and $2\omega_{TN}$ for two species labeled A and B. The nutation frequencies are characterized by the ratio $2\omega_{TN}^{(A)} / 2\omega_{TN}^{(B)} = 9.9 / 6.9 = 1.435 \approx \sqrt{2}$, which corresponds to $S = 1$ and $S = 1/2$ for A and B, respectively. This interpretation was verified by monitoring the variation of $\omega_{TN}^{(A)}$ and $\omega_{TN}^{(B)}$ with the microwave field amplitude B_1. As expected, the two slopes differed by $\sqrt{2}$ [74]. The participation of these two types of radicals to the EPR line was confirmed by recording the two-dimensional PEANUT spectrum, *i.e.* the nutation spectrum as a function of the magnetic field (Fig. 15.16a). The skyline projections along the nutation axis and along the magnetic field axis represent the nutation spectrum and the absorption EPR spectrum, respectively. This 2D-representation clearly demonstrates that both $S = 1$ and $S = 1/2$ radicals contribute to the EPR line in meteoritic IOM.

The presence of only $S = 1/2$ radicals in the IOM in cherts is more difficult to demonstrate because different types of paramagnetic centers overlap with IOM radicals. However, the nutation frequency corresponding to $S = 1/2$ for these well-known defects can be used as reference for the determination of S in organic radicals. Figure 15.16b shows the 2D-PEANUT spectrum at 4 K of the 1880 Myr-old Gunflint chert. At low temperature, the E′ centre of SiO_2 is undetectable (completely saturated), and the cw-EPR spectrum is the superposition of the IOM radical and a defect of the SiO_2 matrix consisting of a hole trapped in a 2p oxygen orbital adjacent to an Al^{3+} ion in an Si^{4+} site, denoted $[AlO_4/h]^0$ centre or $Al_{Si}°$ [26]. The projection of the nutation spectrum along the magnetic field axis shows two distinct EPR spectra. The projection along the nutation axis also shows peaks at ω_{TN} and $2\omega_{TN}$ for

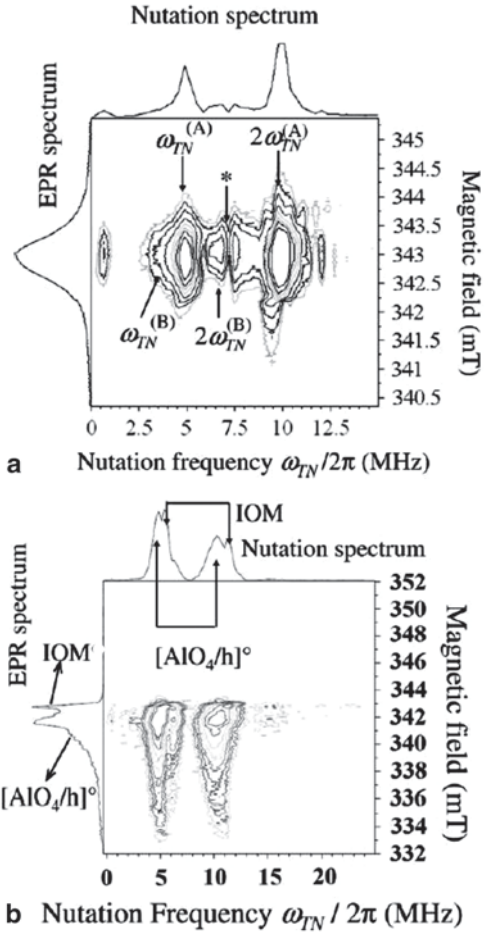

Fig. 15.16 Contour plots of 2D-PEANUT spectra at 4 K of the IOM of the Orgueil meteorite a) and the 1880 Myr-old Gunflint chert b) The narrow feature marked by * in a) is an artifact introduced by the data handling. Adapted from [74] with permission from Elsevier (2011)

the two species. The ratio of their nutation frequencies is equal to $\omega_{TN}^{(1)}/\omega_{TN}^{(2)} = 1.1$, where (1) and (2) represent the IOM radical and the $[AlO_4/h]^0$ centre, respectively. This ratio should be equal to 1 and to $\sqrt{2}$ for IOM radicals with spin 1/2 and 1, respectively. As $2\omega_{TN}^{(2)} = 10$ MHz for the $[AlO_4/h]^0$ centre with $S = 1/2$, we should expect $2\omega_{TN}^{(1)} = 14.1$ MHz (for S = 1) and 10 MHz (for S = 1/2) for the IOM radicals. The experimental value $2\omega_{TN}^{(1)} = 11$ MHz clearly points to a spin value $S = 1/2$ for the fossil IOM. Consequently the presence of $S = 1$ organic radicals is a specificity of extraterrestrial IOM.

15.6.2 The Different Types of Radicals in Meteoritic IOM

More quantitative information on the different types of radicals in meteoritic IOM can be obtained from the temperature dependence of the magnetic susceptibility.

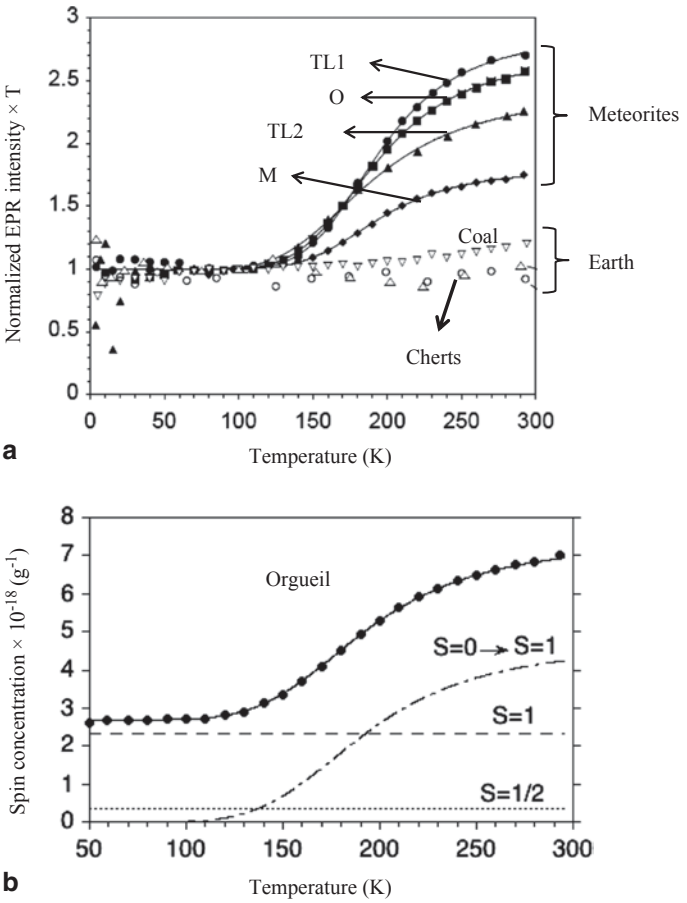

Fig. 15.17 **a** Normalized temperature dependence of the EPR intensity of organic radicals in meteoritic IOM and in fossil IOM. Meteorite samples: Tagish Lake (TL1 and TL2), Orgueil (O) and Murchison (M); Earth samples: a 320 Myr-old coal from Solway Basin, UK, a 1880-Myr-old chert from the Gunflint formation, Canada (*open circles*) and a 3500 Myr-old chert from the Dresser formation, Australia (*open triangles*). Full lines for meteoritic IOM are calculated with Eq. 15.21. Adapted from [39] with permission from Mary Ann Liebert (2013) and from [75] with permission from Elsevier (2004). **b** Simulation (*full line*) of the temperature dependent spin concentration in the Orgueil meteorite by the sum of three components: $S=1/2$ radicals, ferromagnetically coupled $S=1$ diradicals, and antiferromagnetically coupled $S=0$ diradicals with thermally accessible $S=1$ state. Adapted from [74] with permission from Elsevier (2011)

The temperature dependence of the EPR intensity of IOM radicals for different types of materials are shown in Fig. 15.17a). The EPR intensity is multiplied by T to take into account the Curie paramagnetism, and normalized to the intensity at 100K to compare samples with very different radical contents. As expected this normalized intensity is nearly constant for $S=1/2$ radicals of Earth IOM. However, IOM from different meteorites exhibit a significant increase of the normalized EPR intensity, revealing the thermal population of magnetic states from non magnetic ($S=0$)

Table 15.2 Concentrations of the different types of radicals in the IOM of Orgueil meteorite. ΔE and $\Delta\sigma$ are the singlet-triplet splitting and the entropy variation between the two spin states of the antiferromagnetically coupled diradicals, respectivelly. (From [74, 75])

ΔE (cm^{-1})	$\Delta\sigma$ ($cm^{-1}K^{-1}$)	N_1^a (g^{-1})	N_1^f (g^{-1})	$N_{1/2}$ (g^{-1})
816	4.2	1.80±0.005	0.92±0.05	0.24±0.05

states. This has been accounted for by assuming the presence of diradicals with $S=0$ ground state and a thermally accessible triplet state $S=1$ (antiferromagnetic coupling) [75]. This is confirmed by nutation experiments showing the presence of intense $S=1$ nutation frequency peaks at room temperature (Fig. 15.15). However, the presence of a less intense $S=1$ nutation at 4 K indicates also the presence of diradicals with S = 1 ground state (ferromagnetic coupling). The temperature dependence of the spin concentration N per gram of IOM is given by [74, 75]:

$$N = N_{1/2} + \frac{8}{3}N_1^f + \frac{8}{3}N_1^a \frac{1}{1+\exp(-\Delta\sigma / kT)\exp(\Delta E / kT)} \qquad (15.21)$$

where $N_{1/2}$, N_1^f and N_1^a are the spin concentrations for monoradicals, ferromagnetically coupled diradicals and antiferromagnetically coupled diradicals, respectively. $\Delta E = -J$ and $\Delta\sigma$ are the energy splitting and entropy difference, respectively, between $S=1$ and $S=0$ spin states of antiferromagnetically coupled diradicals. The details of the measurements are given in [74, 75]. To compare the behavior of the seven samples, the EPR intensity at each temperature T were normalized with respect to the intensity at 100 K. The results are shown in Fig. 15.17a. For terrestrial IOM, the nearly constant normalized EPR intensity indicates that Equation 15.21 reduces to $N \approx N_{1/2}$. For meteoritic IOM, the solid curves were calculated with very similar values $\Delta E \approx 816$ cm^{-1} (0.10 eV) and $\Delta\sigma \approx 4.2$ $cm^{-1}K^{-1}$ [31, 75]. This indicates that the three meteorites possess the same type of radicals. Absolute spin concentrations in the IOM were calculated for Orgueil meteorite, by assuming that $J >> kT$ for ferromagnetically coupled diradicals. The results are shown in Fig. 15.17b and in Table 15.2. This shows that monoradicals ($S=1/2$) contribute only to ~8% to the radicals in the IOM, while ferromagnetic ($S=1$) and antiferromagnetic ($S=0$) diradicals contribute to ~31% and ~61%, respectively [74].

15.6.3 Nature of Diradicals

Diradicals detected in meteoritic IOM are not fundamentally different from monoradicals of terrestrial IOM, as shown in Sect. 15.3. They are made of polycyclic aromatic units (sp^2 carbons) linked by aliphatic chains (sp^3 carbons). Moreover, ^{1}H- and ^{13}C HYSCORE spectra of meteoritic IOM are very similar to those of partially carbonized organic molecules [39]. From DFT and extended Hückel (EH) calculations, a model was first proposed for these diradicals, based on diradicaloid species hosted by aromatic structures of 10–15 rings and having a quinoidal structure [75].

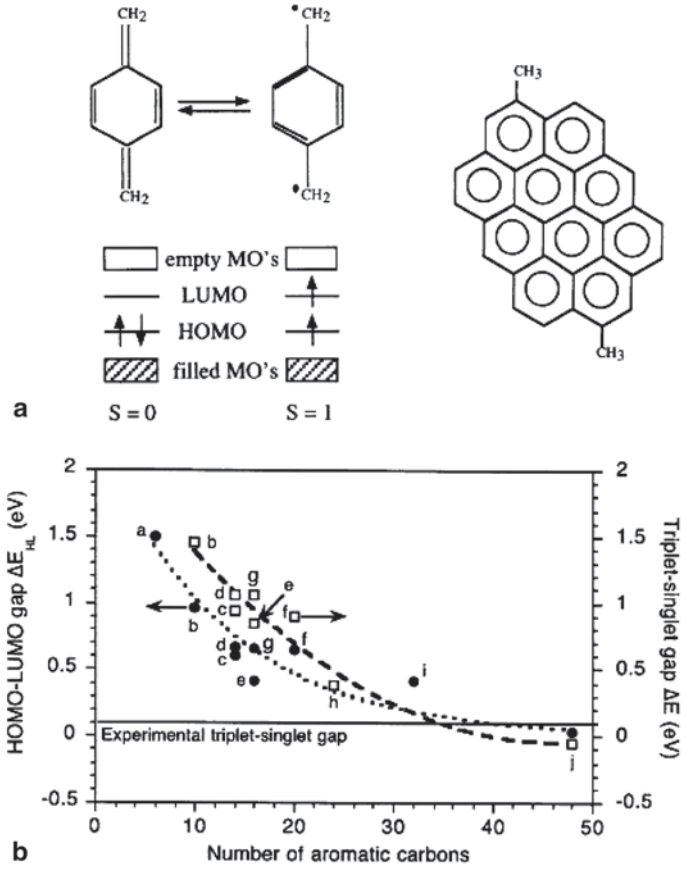

Fig. 15.18 **a** Left: description of a diradical with quinoidal structure (diradicaloid), showing the HOMO-LUMO gap and the two spin states $S=0$ and $S=1$; Right: example of model structure (molecule (i) used for the calculation of the singlet-triplet splitting ΔE and the HOMO-LUMO gap ΔE_{HL}. **b** Variation of ΔE (*open squares*) and ΔE_{HL} (*full circles*) with the number of aromatic carbons in polycyclic aromatic units. ΔE was calculated by DFT method, and ΔE_{HL} by extended Hückel method. Letters represent the molecules. Adapted from [75] with permission from Elsevier (2004)

The two spin states of a diradical with quinoidal structure (diradicaloid) are represented on Fig. 15.18a, with the example of a simple benzene ring [75]. Calculations were performed on model polycyclic aromatic units with variable number of rings and variable shapes, where aliphatic branching is simulated by two $-CH_3$ groups (Fig. 15.18a). The variations with the number of aromatic carbon atoms of the singlet-triplet (ST) spitting ΔE (calculated by DFT method), and of the HOMO-LUMO (HL) gap (calculated by the EH method) are shown in Fig. 15.18b. A positive (negative) ST gap means that the $S=0$ ($S=1$) state is the ground state, which corresponds to an antiferromagnetically (ferromagnetically) coupled diradicaloid. These calculations show that the experimental value of the ST gap $\Delta E \approx 0.1$ eV (ground

state $S=0$) is obtained for molecules containing about 30–40 aromatic carbon atoms (10–15 fused benzene rings), while molecules with more than about 40 aromatic carbon atoms have an $S=1$ ground state. These calculations indicate also that the two types of diradicals found in meteoritic IOM may be of the same type, differing only by the sizes of the polyaromatic group. The fact that the same values of ΔE and $\Delta\sigma$ are measured for three meteorites of different origin in the solar system (Orgueil, Murchison, Tagish Lake), strongly suggests that the antiferromagnetically coupled diradicals have a well defined size. As diradicals represent more than 98 % of the radicals in the Orgueil meteorite, and the fact that it was quantitatively demonstrated that radicals (of all types) are the carriers of the deuterium excess [62], we may conclude that diradicals are responsible for the major deuterium excess in IOM. We may also expect that diradicaloids with much less than ~10 fused rings would exhibit an ST gap much larger than 0.10 eV, and thus would be EPR silent. Such small diradicaloids are not present in the IOM because this would imply that non magnetic organic molecules are also the carriers of deuterium excess, which is not the case.

Although the diradicaloid model accurately explains most of the experimental features, it suffers from a major drawback which is the very high instability of these species, except in some exceptional cases [76]. It was argued that the very high chemical stability of the IOM could protect these reactive diradicaloids against destructive reactions [75]. However this was only a working hypothesis.

An alternative model may appear more likely, which possesses the same characteristics as the diradicaloid model, *ie* a ST gap with size and sign which depends on the number of fused rings in the polyaromatic radical, without the instability problem of diradicaloids. The recent achievements in chemistry, physics and technology of graphene have revealed the unconventional electronic properties of this family of materials [77]. The so-called nanographene of physicists is nothing else than a hydrogenated polyaromatic carbon molecule for chemists. Decreasing the size of graphene to the nanometer range results in an increasing contribution of edge states (zigzag edges and armchair edges, see Fig. 15.19) for the electronic structure ([78–83] and references therein). Although the details are model dependent, it has been found that upon increasing the size of polyaromatic groups, the electronic structure evolves from a close shell singlet ($S=0$) ground state to an open shell singlet diradical ground state and next to a triplet diradical ($S=1$) ground state. The spin density is localized on zigzag edges, with one spin on one edge and the other spin on the other edge (Fig. 15.19). Elongation of the zigzag edge increases the diradical character whereas elongation of the armchair edge decreases the diradical character [81]. As expected, the HOMO-LUMO gap decreases upon increasing the zigzag edge length N (number of benzene rings) and the singlet-triplet transition in diradicals occurs for $N\approx 5$–8, depending on the length of the armchair edge and the shape of the nanographene sheet [81, 83]. This nanographene model appears more likely than the diradicaloid model, as the singlet and triplet diradical states are a direct consequence of the polyaromatic character of the molecule in the nanographene model, whereas homolytic breaking of the C-H bond in benzylic position in branching aliphatic chains are necessary to give a diradicaloid [75]. The common feature of these two models is that singlet to triplet transition in diradicals is induced

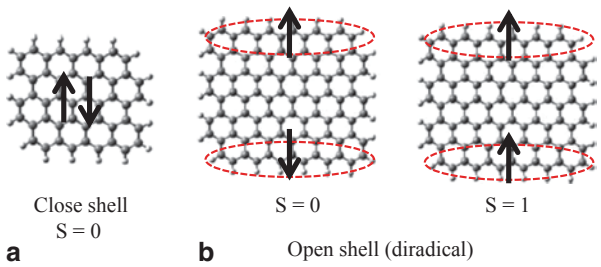

Fig. 15.19 Schematic representation of the spin distribution upon increasing the size of a nanographene sheet; **a** close shell S = 0 character for small size; **b** transition to open shell diradical state above a critical size (model dependent); The spin density becomes localized on *zigzag edges*. For moderate size, S = 0 state is lowest (antiferromagnetic coupling). Upon further increasing size, the singlet-triplet gap decreases and S = 1 state is lowest above a second critical size (ferromagnetic coupling)

upon increasing the size of the polyaromatic core. The fact that diradicals with the two types of ground state (singlet and triplet) represent the major part of deuterium carriers in meteoritic IOM, points out that deuterium is localized mostly on large polyaromatic molecules with two different sizes. As deuterium is an important marker in Astrochemistry, further work must focus on these diradicals to get deeper insight into the history of organic matter in the Early solar system.

15.7 Conclusion

Carbonaceous matter with an age in the range ~1–4.5 billion years contains paramagnetic radicals that record the history of the primitive organic matter, stored in the various interactions of the electron spins with surrounding atoms. This history started with the formation of the solar system (origin of the organic matter) and includes the apparition of life. Various information can be recovered by combining EPR methodologies, among which the origin (biologic versus abiotic) of the fossil organic matter, the age of the organic matter with respect to that of the host rock (syngeneity versus contamination), and the origin of the deuterium enrichment of extraterrestrial organic matter. EPR thus appears an emerging tool for tracking the first traces of life on Earth or on returned rocks from future Mars missions.

References

1. Westall W (2008) Morphological biosignatures in early terrestrial and extraterrestrial materials. Space Sci Res 135:95–114
2. Ehrenfreund P, Rasmussen S, Cleaves J, Chen L (2006) Experimentally tracing the key steps in the origin of life: the aromatic world. Astrobiology 6:490–520

3. Roeder E (1981) Are the 3800-Myr-old Isua objects microfossils, limonite-stained fluid inclusions, or neither? Nature 293:159–162
4. Knoll AH, Golubic S, Green J, Swett K (1986) Organically preserved microbial endoliths from the late Proterozoic of East Greenland. Nature 321:856–857
5. Westall W, Folk RL (2003) Exogenous carbonaceous microstructures in Early Archean cherts and BIFs from the Isua Greenstone Belt: implications for the search for life in ancient rocks. Precambrian Res 126:313–330
6. Garcia-Ruiz JM, Hyde ST, Carnerup AM, Christy AG, van Kranendonk MJ, Welham NJ (2003) Self-assembled silica-carbonate structures and detection of ancient microfossils. Science 302:1194–1197
7. Hayatsu R, Matsuoka S, Scott RG, Studier MH, Anders E (1977) Origin of the organic matter in the early solar system, VII: the organic polymers in carbonaceous chondrites. Geochim Cosmochim Acta 41:1325–1339
8. Chyba C, Sagan K (1992) Endogenous production, exogenous delivery andimpact-shock synthesis of organic molecules: an inventory for the origin of life. Nature 355:125–132
9. Summons RF, Amend JP, Bish D, Buick R, Cody GD, Des Marais DJ, Dromart G, Eigenbrode JL, Knoll AH, Sumner DY (2011) Preservation of Martian organic and environmental records: final report of the Mars Biosignature Working Group. Astrobiology 11:157–181
10. Bibring J-P, Langevin Y, Gendrin A, Gondet B, Poulet F, Berthe M, Soufflot A, Arvidson R, Mangold N, Mustard J, Drossart P, and the Omega team (2005) Mars surface diversity as revealed by the OMEGA/Mars Express observations. Science 307:1576–1581
11. Mojzsis ST, Arrhenius G, McKeegan KD, Harrison TM, Nutman AP, Friend CRI (1996) Evidence for life on Earth before 3,800 million years ago. Nature 384:55–59
12. Brasier MD, Green OR, Jephcoat AP, Kleppe AT, van Kranendonk MJ, Lindsay JF, Steele A, Grassineau NV (2002) Questioning the evidence for earth's oldest fossils. Nature 416:76–81
13. Schopf JW, Kudryavtsev AB (2012) Biogenicity of earth's earliest fossils: a resolution of the controversy. Gondwana Res 22:761–771
14. Krot AN, Hutcheon ID, Brearley AJ, Pravdivtseva OV, Petaev MI, Hohenberg CM (2006) In Meteorites and the early solar system II (eds Lauretta D and McSween HYJJ). University of Arizona Press, Tucson, p 525
15. Huss GR, Rubin AE, Grossman JN (2006) In Meteorites and the early solar system II (eds Lauretta D and McSween HYJJ). University of Arizona Press, Tucson, p 567
16. Robert F, Epstein S (1982) The concentration of isotopic compositions of hydrogen carbon and nitrogen in carbonaceous chondrites. Geochim Cosmochim Acta 16:81–95
17. Alexander CMO'D, Fogel M, Yabuta H, Cody GD (2007) The origin and evolution of chondrites recorded in the elemental and isotopic compositions of their macromolecular organic matter. Geochim Cosmochim Acta 71:4380–4403
18. Remusat L, Palhol F, Robert F, Derenne S (2006) Enrichment of deuterium in insoluble organic matter from primitive meteorites: a solar system origin? Earth Planet Sci Lett 243:15–25
19. Pflug HD, Jaeschke-Boyer H (1979) Combined structural and chemical analysis of 3,800-Myr-old microfossils. Nature 280:483–486
20. Marschall CP, Marschall AO (2013) Raman hyperspectral imaging of microfossils: potential pitfalls. Astrobiology 13:920–993
21. Vago J, Gardini B, Kminek G, Baglioni P, Gianfiglio G, Santovicenzo A, Bayon S, van Winendael M (2006) ExoMars-searching for life on the red planet. ESA Bull 126:16–23
22. Gourier D, Delpoux O, Skrzypczak-Bonduelle A, Binet L, Ciofini I, Vezin H (2010) EPR, ENDOR and HYSCORE study of the structure and the stability of vanadyl-porphyrin complexes encapsulated in silica : potential paramagnetic biomarkers for the origin of life. J Phys Chem B 114:3714–3725
23. Kim SS, Bargar J, Nealson KH, Flood B, Kirschvink J, Raub T, Tebo B, Villalobos M (2011) Searching for biosignatures using electron paramagnetic resonance (EPR) analysis of manganese oxides. Astrobiology 11:775–786

24. Vandenbroucke M, Largeau C (2007) Kerogen origin, evolution and structure. Organic Geochem 38:719–833
25. Marchand A, Conard J (1980), Electron paramagnetic resonance in kerogen studies. In: Durand B (ed) Kerogen: Insoluble organic matter from sedimentary rocks. Technip, Paris, pp 243–270
26. Skrzypczak-Bonduelle A, Binet L, Delpoux O, Vezin H, Derenne S, Robert F, Gourier D (2008) EPR of radicals in primitive organic matter: a tool for the search of biosignatures of the most ancient traces of life. Appl Magn Reson 133:371–397
27. Villée F, Duchesne J, Depireux J (1964) Radicaux libres dans les météorites carbonées. CR Acad Sci Paris 258:2376–2379
28. Schulz KF, Elofson RM (1965) Electron spin resonance studies of organic matter in the Orgueil meteorite. Geochim Cosmochim Acta 29:157–160
29. Binet L, Gourier D, Derenne S, Robert F (2002) Heterogeneous distribution of paramagnetic radicals in insoluble organic matter from the Orgueil and Murchison meteorites. Geochim Cosmochim Acta 66:4177–4186
30. Silbernagel BG, Gebhard LA, Dyrkacz GR (1984) ESR of carbon radicals in isolated coal macerals. In: Petrakis L and Fraissard J-P (eds) Magnetic resonance, introduction, advanced topics and applications to fossil energy. Reidel, Dortrecht, pp 645–653
31. Binet L, Gourier D, Derenne S, Pizarello S, Becker L (2004) Diradicaloids in the insoluble organic matter from the Tagish lake meteorite: comparison with the Orgueil and Murchison meteorites. Meteoritic Planetary Science 39:1649–1616
32. Singer LS, Lewis IC (1978) ESR study of the kinetics of carbonization. Carbon 16:417–423
33. Carniti P, Beltrame PL, Gervasini A, Castelli A, Bergamasco L (1997) Formation of radicals in thermal degradation of kerogen. A kinetic study. J Anal Appl Pyrolysis 40–41:553–568
34. Mrozowski S (1988) ESR studies of carbonization and coalification processes part II: biological materials. Carbon 26:531–541
35. Abragam A (1961) Principle of nuclear magnetism. Clarendon, Oxford
36. Bourbin M, Derenne S, Gourier D, Rouzaud J-N, Gautret P, Westall F (2012) Electron paramagnetic resonance study of a photosynthetic microbial mat and comparison with Archean cherts. Orig Life Evol Biosph 42:569–485
37. Wertz JE, Bolton JR (1986) Electron spin resonance: elementary theory and applications. Chapman & Hall, London
38. Gourier D, Robert F, Delpoux O, Binet L, Vezin H, Moissette A, Derenne S (2008) Extreme deuterium enrichment of organic radicals in the Orgueil meteorite: revisiting the interstellar interpretation? Geochim Cosmochim Acta 72:1914–1923
39. Gourier D, Delpoux O, Binet L, Vezin H (2013) Nuclear magnetic biosignatures in the carbonaceous matter of ancient cherts: comparison with carbonaceous meteorites. Astrobiology 13:932–947
40. Fel'dman EB, Lacelle S (1996) Configurational averaging of dipolar interactions in magnetically diluted spin networks. J Chem Phys 104:2000–2009
41. Bourbin M, Gourier D, Derenne S, Binet L, Le Du Y, Westall F, Kremer B, Gautret P (2013) Dating carbonaceous matter in Archean cherts by electron paramagnetic resonance. Astrobiology 13:151–162
42. Derenne S, Robert F (2010) Model of molecular structure of the insoluble organic matter isolated from Murchison meteorite. Meteorit Planet Sci 45:1461–1475
43. Schweiger A, Jeschke G (2001) Principle of pulsed electron paramagnetic resonance. Oxford University Press, Oxford
44. Höfer P, Grupp A, Nebenfürh H, Mehring M (1986) Hyperfine sublevel correlation (HYSCORE) spectroscopy: a 2D ESR investigation of squaric acid radical. Chem Phys Lett 132:279–282
45. Rowen LG, Hahn EL, Mims WB (1965) Electron spin echo modulation. Phys Rev 137:A61–A71
46. Anderson MW, Kevan LJ (1986) Electron spin resonance and electron spin echo study of Cu^{2+} in zeolites H-RHO and CSH-RHO. J Phys Chem 90:6452–66459

47. Gerson F, Huber W (2003) Electron spin resonance spectroscopy of organic radicals. Wiley, Weinheim
48. Gordy W (1980) Theory and application of electron spin resonance. Wiley, New York
49. Pöppl A, Kevan L (1996) A practical strategy for determination of proton hyperfine interaction parameters in paramagnetic transition metal ion complexes by two-dimensional HYSCORE electron spin resonance spectroscopy in disordered systems. J Phys Chem 100:3387–3394
50. Gardinier A, Derenne S, Robert F, Behar F, Largeau C, Maquet J (2000) Solid state CP/MAS ^{13}C NMR of the insoluble organic matter of the Orgueil and Murchison meteorites: quantitative study. Earth Planet Sci Lett 184:9–21
51. Cody GD, Alexander CMO'D (2005) NMR studies of chemical structural variation of insoluble organic matter from different carbonaceous chondrite groups. Geochim Cosmochim Acta 69:1085–1097
52. Ikoma T, Ito O, Tero-Kubota S, Akiyama K (1998) HYSCORE study on coal radicals. Energy Fuels 12:1363–1368
53. Ikoma T, Ito O, Tero-Kubota S (2002) Exploring radicals in carbonaceous solids by means of pulsed EPR spectroscopy. Energy Fuels 16:40–47
54. Durand B, Nicaise G (1980) Procedures for kerogen isolation, in Kerogen (edited by Durand B). Technip, Paris, pp 35–53
55. Jefferts KB, Penzias AA, Wilson RW (1973) Deuterium in the Orion Nebula. Astrophys J 179:L57–L61
56. Geiss J, Reeves H (1972) Cosmic and solar system abundances of deuterium and helium-3. Astron Astrophys 18:126–132
57. Mahaffy PR, Donahue TM, Atreya SK, Owen TC, Niemann HB (1998) Galileo probe measurements of D/H and $^{3}He/^{4}He$ in Jupiter's atmosphere. Space Sci Res 84:251–263
58. Brown PD, Millar TJ (1989) Models of the gaz-grain interaction-D chemistry. Monthly Notices R Astron Soc 237:661–671
59. Halbout J, Robert F, Javoy M (1990) Hydogen and oxygen isotope compositions in kerogens from the Orgueil meteorite: clues to the solar origin. Geochim Cosmochim Acta 54:1453–1462
60. Kerridge JF (1985) Carbon, hydrogen and nitrogen in carbonaceous meteorites: abundances and isotopic compositions in bulk samples. Geochim Cosmochim Acta 49:1707–1714
61. Busemann H, Young AF, Alexander CM, Hoppe P, Mukhopadhyay S, Nittler LR (2006) Interstellar chemistry recorded in organic matter from primitive meteorites. Science 312:727–730
62. Remusat L, Robert F, Meibom A, Mostefaoui S, Delpoux O, Binet L, Gourier D, Derenne S (2009) Proto-planetary disk chemistry recorded by D-rich organic radicals in carbonaceous chondrites. Astrophys J 698:2087–2092
63. Glassgold A, Feigelson ED, Montmerle T (2000) Effects on energetic radiation in young stellar objects. In: Mannings V, Boss AP and Russel SS (eds) Protostars and planets IV. University Arizona Press, Arizona, pp 429–455
64. Zhang XM (1998) Homolytic bond dissociation of the C–H bonds adjacent to radical centers. J Org Chem 63:1872–1877
65. Remusat L, Ghan Y, Wang Y, Eiler JM (2010) Accretion and preservation of D-rich organic particles in carbonaceous chondrites: evidence for important transport in the early solar system nebula. Astrophys J 713:1048–1058
66. Retcovsky HL, Hough MR, Maguire MM, Clarckson RB (1981) Nature of the free radicals in coals, pyrolyses coals, solvent-refined coals and coal liquefaction products. In Coal Structure. Am Chem Soc Advances in Chem Series, 192, n°4, pp 37–58
67. Conard J (1984) EPR in fossil carbonaceous materials. In: Petrakis L, Fraissard JP (eds) Magnetic resonance, introduction, advanced topics and application to fossil energy. Reidel, Dortrecht, pp 441–459
68. Rothenberger KS, Sprecher RF, Castellano SM, Retcovsky HL (1993) Temperature dependence of the electron paramagnetic resonance intensity of whole coals. In: Botto RE, Sanada

Y (eds) Magnetic resonance of carbonaceous solids, vol 299 (Advances in Chemistry Series). American Chemical Society, Washington, DC
69. Barklie RC, Collins M, Silva SRP (2000) EPR linewidth variation, spin relaxation times, and exchange in amorphous hydrogenated carbon. Phys Rev B 61:3546–3554
70. Robertson J (2002) Diamond-like amorphous carbon. Mater Sci Eng R37:129–281
71. Astashkin AV, Schweiger A (1990) Electron-spin transient nutation: a new approach to simplify the interpretation of ESR spectra. Chem Phys Lett 174:595–602
72. Solomon I (1959) Rotary spin echoes. Phys Rev Lett 2:301–302
73. Stoll S, Jeschke G, Willer M, Schweiger A (1998) Nutation frequency correlated EPR spectroscopy: the PEANUT experiment. J Magn Reson 130:86–96
74. Delpoux O, Gourier D, Vezin H, Binet L, Derenne S, Robert F (2011) Biradical character of D-rich carriers in the insoluble organic matter of carbonaceous meteorites: a relic of the protoplanetary disk chemistry. Geochim Cosmochim Acta 75:326–336
75. Binet L, Gourier D, Derenne S, Robert F, Ciofini I (2004) Occurrence of abundant diradicaloid moieties in the insoluble organic matter from the Orgueil and Murchison meteorites: a fingerprint of its extraterrestrial origin? Geochim Cosmochim Acta 68:881–891
76. Jung Y, Head-Gordon M (2003) How diradicaloid is a stable diradical? Chem Phys Chem 4:522–525
77. Geim AK, Novoselov KS (2007) The rise of grapheme. Nat Mater 6:183–191
78. Fernandez-Rossier J, Palacios JJ (2007) Magnetism in grapheme nanoislands. Phys Rev Lett 99(177204):1–4
79. Philpott MR, Kawazoe Y (2009) Bonding and magnetism in nanosized grapheme molecules: Singletstates of zigzag edged hexangulenes $C_{6m}H_{6m}$ (m=2,3, …,10). J Chem Phys 131(214706):1–12
80. Enoki T, Takai K (2009) The edge state of nanographene and the magnetism of the edge-state spins. Solid State Comm 149:1144–1150
81. Wang J, Zubarev DY, Philpott MR, Vukovic S, Lester WA, Cui T, Kawazoe Y (2010) Onset of diradical character in small nanosized grapheme patches. Phys Chem Chem Phys 12:9839–9844
82. Philpott MR, Kawazoe Y (2011) Triplet states of zigzag edged hexagonal grapheme molecules $C_{6m}2H_{6m}$ (m=1,2,3,…,10) and carbon based magnetism. J Chem Phys 134(124706):1–9
83. Pham BQ, Truong TN (2012) Electronic spin transitions in finite-size graphene. Chem Phys Lett 535:75–79